

© 2020 Ram Sai Gorugantu

DESIGN AND IMPLEMENTATION OF HIGH-BANDWIDTH,
HIGH-RESOLUTION IMAGING IN ATOMIC FORCE MICROSCOPY

BY

RAM SAI GORUGANTU

DISSERTATION

Submitted in partial fulfillment of the requirements
for the degree of Doctor of Philosophy in Mechanical Engineering
in the Graduate College of the
University of Illinois at Urbana-Champaign, 2020

Urbana, Illinois

Doctoral Committee:

Professor Srinivasa M. Salapaka, Chair and Director of Research
Professor Naira Hovakimyan
Professor Kimani C. Toussaint, Brown University
Professor Petros G. Voulgaris

ABSTRACT

Video-rate imaging with subnanometer resolution without compromising on the scan range has been a long-awaited goal in Atomic Force Microscopy (AFM). The past decade saw significant advances in hardware used in atomic force microscopes, which further enable the feasibility of high-speed Atomic Force Microscopy. Control design in AFMs plays a vital role in realizing the achievable limits of the device hardware. Almost all AFMs in use today use Proportional-Integral-Derivative(PID) control designs, which can be majorly improved upon for performance and robustness. We address the problem of AFM control design through a systems approach to design model-based control laws that can give major improvements in the performance and robustness of AFM imaging.

First, we propose a cascaded control design approach to tapping mode imaging, which is the most common mode of AFM imaging. The proposed approach utilizes the vertical positioning sensor in addition to the cantilever deflection sensor in the feedback loop. The control design problem is broken down into that of an inner control loop and an outer control loop. We show that by appropriate control design, unwanted effects arising out of model uncertainties and nonlinearities of the vertical positioning system are eliminated. Experimental implementation of the proposed control design shows improved imaging quality at up to 30% higher speeds.

Secondly, we address a fundamental limitation in tapping mode imaging by proposing a novel transform-based imaging mode to achieve an order of magnitude improvement in AFM imaging bandwidth. We introduce a real-time transform that effects a frequency shift of a given signal. We combine model-based reference generation along with the real-time transform. The proposed method is shown to have linear dynamical characteristics, making it conducive for model-based control designs, thus paving the way for achieving superior performance and robustness in imaging.

To Sri Sri Ravishankar, and to my parents, for their love and support.

ACKNOWLEDGMENTS

I am deeply grateful to Prof. Vasu Salapaka for allowing me to work with him. Throughout this period, I felt unconditionally supported by him. I am also grateful to him for giving me ample space to learn and grow. The one thing I have come to appreciate the most in him is the spirit of choosing challenging yet impactful problems and persisting through to completion. Had it not been for the transient nature of the Ph.D. program, I would have loved to continue working on these problems. It was a privilege to have eminent professors on my doctoral committee. I would like to thank my committee members, Prof. Naira Hovakimyan, Prof. Kimani Toussaint, and Prof. Petros Voulgaris, for reviewing my work and for their valuable inputs. I would like to specially acknowledge my lab mates, Mayank, and Mashrafi for working with me and supporting this work during different phases. I would also like to acknowledge Gayathri Mohan, Yunwen Xu, Amber Srivastava, Alireza Askarian, Pratik Parikh, Yuchen Xu, Sreenath Sundar, Raj Kiriti Velicheti and Jaesang Park who have contributed to my learning experience as lab-mates. Apart from research, the opportunities to interact with world-class professors and learn from them are valuable to me.

I am happy to have gone through the Ph.D. experience, which has been a learning experience beyond what I could have imagined. I would like to acknowledge my uncle, Late Prof. N.Someswara Rao, and my cousin-in-law Late Prof. Chandrasekhar Pammi for setting great examples, that also inspired me to make the choice of pursuing a Ph.D.

I have met some of the most awesome friends at UIUC. I would like to mention about the memorable times I had, especially with Ravi Agarwal, Kaushik Sankar, Mayank Baranwal, Mansi Agarwal, Krishna Kalyan Medarametla, Shivangi Prasad, Harpreet Kaur, Geethika Yalamanchili, Sindhu Velagala, and many more friends, especially in the first few years. Also, support from some of my Champaign community friends, including Laxmi Rao, Ravi Kan-

dasamy, and Heena Pitchaikani helped me feel totally at home in Chambana very quickly after I moved in.

I am grateful to have some all-weather mentors and friends in Siva Theja Maguluri, Srikanthan Sridharan, and Venkat Srinivasan. Interactions with these people have elevated my perspectives on many aspects of life and also have given me immense strength. I feel sorry to have lost Chaitanya Sathe, who was a very dear friend and mentor.

It was an enriching experience to be a part of SKY at UIUC, where I met some of the most amazing friends. It was amazing to see the group, strung together by a quest for inner freedom, grow both in terms of size and also in terms of individual growth. It's mind-boggling how the group went on to become widely recognized on campus within just a few years of setting up. This community has provided me with great mental nourishment, which is much needed while pursuing a Ph.D. I am grateful to each and everyone at SKY at UIUC, especially I would like to mention Ghazal Bhatia, Krishna Anapindi, Abhishek Sharma, Christina Tang, Puja Goyal, Mergen Gerelbat, Arati Paudel, Amrita Kataruka, Sreekalyan Patiballa, Sri-raam Chandrasekaran, Srividhya Sriraam, Varenya Mehta, Shivani Bhalla, and Puja Paudel, among many more people whom I have come to share a close bond with. It was an amazing experience to lead meditation sessions across campus. I am grateful for the mentorship of Shyam Gannavaram, Annelies Richmond, and Nina Sanyal, who traveled from across the country to facilitate SKY happiness retreats. These opportunities leave me feeling contented for being able to contribute towards the wellbeing of the campus community and also have strengthened me in an indescribable way.

I am grateful for having the luxury of having cousins living in the same country. I am happy to have the opportunities to meet-up with my cousins Sriya, Raghav, and Subbu and their families. Subbu and Rashmi moving to Chicago during the final phase of the Ph.D. was a great support during challenging times.

I am grateful to my parents, for the unconditional love and support, which is beyond the realm of expression. I am also deeply grateful to my spiritual master, Sri Sri Ravishankar, for showing me ways to find my inner peace and happiness, independent of external situations. His presence has given me so much abundance that I am inspired to facilitate the same for others.

TABLE OF CONTENTS

LIST OF FIGURES	viii
CHAPTER 1 INTRODUCTION	1
1.1 Video-rate AFM imaging: Motivation	1
1.2 Approaches Employed	3
1.3 Scope of the thesis	4
1.4 Organization of the thesis	5
CHAPTER 2 ATOMIC FORCE MICROSCOPY	6
2.1 Historic Overview	6
2.2 Principle of AFM	6
2.3 Imaging modes	7
2.4 Cantilever Model	10
2.5 Control of AFM imaging	13
CHAPTER 3 ENABLING HARDWARE	16
3.1 Electronics	16
3.2 Nanopositioning stages	21
3.3 Enhanced AFM setup	24
3.4 Conclusion	24
CHAPTER 4 FAST TAPPING-MODE IMAGING USING MULTIPLE SENSORS	28
4.1 Problem Formulation	30
4.2 Control design	33
4.3 Inner-loop control using Glover-McFarlane robust loop-shaping	35
4.4 Outer-loop control for amplitude regulation in tapping-mode imaging	39
4.5 Experimental Results	42
4.6 Conclusion	47
CHAPTER 5 A NOVEL TRANSFORM-BASED HIGH-BANDWIDTH AFM IMAGING MODE	50
5.1 Design Framework	51
5.2 Real-time frequency shifting transform	54

5.3	Control Design	56
5.4	Simulations	60
5.5	Conclusion	64
CHAPTER 6 CONCLUSIONS AND FUTURE DIRECTIONS		65
REFERENCES		67

LIST OF FIGURES

2.1	Schematic of an Atomic Force Microscope	8
2.2	Contact mode imaging	9
2.3	Tapping Mode imaging	11
2.4	Effects of thermal noise on dynamic mode imaging	12
2.5	Tip-Sample interaction Force vs Distance	14
2.6	A typical experimental force curve	14
3.1	FPAAs peak detection at 100Hz (top) and 1kHz(bottom)	19
3.2	Noise-Speed tradeoff in FPAAs peak detection	19
3.3	Tapping mode imaging: Amplitude detection and PID control	20
3.4	Tapping mode image of a calibration grid using peak detection	21
3.5	Contact mode imaging:PID control	22
3.6	Contact mode imaging of a calibration grid using FPAAs based control	23
3.7	Custom designed plate-piezo based vertical nanopositioner hardware	25
3.8	(a) NI USB 7855R for implementing advanced controllers (b) Direct form 2 implementation of biquad blocks with two delay elements	26
4.1	Schematic for cascaded control approach	29
4.2	Block diagram schematic for the modified inner- z piezo actuator	31
4.3	Experimental frequency response of the vertical z -piezo actuator in MFP-3D AFM	33
4.4	A Glover-McFarlane robust loop-shaping control framework with pre-compensator W_1	35
4.5	Bode-plots of the open-loop, and the closed-loop plants	37
4.6	Experimental tracking response of the FPAAs based implementation of Glover-McFarlane robust loop-shaping control design for the vertical z -piezo actuator	38
4.7	Power spectrum of z -sensor noise	39
4.8	Block diagram representation of control scheme for tapping-mode imaging.	40
4.9	Experimental frequency response for the plant G_{zA}	41
4.10	Closed-loop frequency responses for the case of hard-engagement	43

4.11	Closed-loop transfer functions for the case of soft-engagement	44
4.12	Complementary sensitivity and sensitivity transfer functions for the closed-loop control of contact-mode imaging	45
4.13	Section scans of a calibration grating	46
4.14	Imaging results at different scan-speeds and set-points - with inner-loop control	48
4.15	Low-speed scan revealing the presence of anomalies in the calibration grating	49
5.1	Simplified Spring-Mass-Damper model of an AFM cantilever. .	52
5.2	Schematic of the error system with \tilde{p} as output	54
5.3	Response of the system to fixed-frequency sinusoidal input . .	56
5.4	Frequency Responses from q to \tilde{p}_β obtained for different white-noise amplitudes	57
5.5	Closed-loop feedback diagram	58
5.6	Closed-loop system with weighting functions for the stacked \mathcal{H}_∞ control design	60
5.7	Closed-loop transfer functions S and T	61
5.8	Tracking performance of a PID controller with linear model-based tuning	62
5.9	Tracking performance of the \mathcal{H}_∞ -optimal controller for filtered white noise and step features	62
5.10	Tracking performance of the \mathcal{H}_∞ -optimal controller for 40nm peak-peak amplitude feature	63
5.11	Tracking performance of the \mathcal{H}_∞ -optimal controller for 10nm peak-peak amplitude feature	63

CHAPTER 1

INTRODUCTION

This thesis explores tools and techniques to enable fast imaging in Atomic Force Microscopes(AFM), towards the goal of achieving video-rate AFM imaging. We employ hardware advances combined with advanced control design techniques to significantly improve the speed of AFM imaging while maintaining high resolution of imaging. First, we show improvement in imaging quality at up to 30% faster speed by using a cascaded control approach and concepts from robust control theory. Consequently, we address a fundamental limitation in an existing imaging technique and propose a novel transform-based imaging method, that gives a close to linear input-output relationship, paving the way for the use of advanced linear robust control approaches such as \mathcal{H}_∞ -optimal control.

The rest of this chapter is organized as follows. In section 1.1, we motivate the need for video-rate AFM imaging. In section 1.2, we discuss the approaches used in this thesis. Finally in sections 1.3 and 1.4, we present the scope and organization of this thesis.

1.1 Video-rate AFM imaging: Motivation

The Atomic Force Microscope [1] is a powerful, high-resolution imaging tool that has a tremendous impact in diverse areas of science and technology, such as biology, materials science, and physics. In 1996, researchers showed that the resolution of an AFM could be high enough to image individual atoms under appropriate conditions[2]. To this day, AFMs continue to push the limits in terms of investigation at nanoscale and subnanoscale. Recently, nanoscientists were able to resolve electron interactions in 8-hydroxyquinoline to the extent that they were able to observe fine tendril-like features where hydrogen bonds are expected to form[3]. The physical limit of achievable

resolutions for AFMs is about a tenth of an angstrom. With substantial progress in pushing limits of achievable resolution in AFM imaging, today, AFM researchers are focused on pushing the limits in terms of the speed of imaging. While very high resolutions have already been achieved, a lot needs to be done to improve the speed of AFM imaging.

High-speed AFM imaging will allow imaging of dynamic phenomena at the nanoscale. This will have a significant impact in a number of applications. For example, observing motor protein transport in living cells [4] can be enabled by high-speed AFM. This could have the impact of deepening our understanding of these phenomena, which in turn could advance further research in understanding diseases such as Alzheimer's disease. Another major area which high-speed AFM imaging would impact is the study of materials. Typically studies in material science such as studying corrosion behavior require high areas of imaging. High imaging rates over high scan area will further these studies in a major way as AFMs offer superior resolution in comparison with Scanning Electron Microscopes(SEMs), which are currently used for these studies. In addition, high-speed AFM also opens up the possibility of observing these processes in real-time and thus can offer extremely valuable insights into how these processes catalyze and progress[5].

The current state of the art solutions in high-speed AFM imaging offer imaging of extremely small scan areas of the order of few nanometers in length at high speeds of a few images per second. The goal of imaging large areas at video-rate is of major interest to AFM researchers. To accomplish this goal, we will need major improvements in various aspects of AFM imaging. One area of improvement is the use of non-raster scans for imaging. Most current AFMs use the raster scanning method to obtain the sample topography. However, raster scanning methods use up a considerable fraction of precious imaging time outside the area of interest. Researchers have been developing non-raster scan imaging techniques based on lissajous,spiral and cycloid trajectories [6],[7],[8],[9]. Another area of improvement is the use of cantilever arrays instead of a single cantilever probe to simultaneously image multiple scan lines at a time[10],[11],[12]. Another area of improvement that we address in this thesis is the use of advanced hardware for nanopositioning and control, combined with the use of advanced control design techniques. We outline our approach in the following section.

1.2 Approaches Employed

In this thesis, we address the challenge of improving AFM imaging speed by the use of a comprehensive systems-based approach for control design in combination with nanopositioning stages capable of scanning at higher bandwidths. We outline these approaches below.

1.2.1 Systems based approach for AFM control design

Control design is an important aspect of AFM operation. A well-designed control system can significantly enhance the spatial and temporal performance of AFM imaging. While PID control approaches provide the versatility of feedback control to any application, they are very sensitive to variation in system properties and also leave a lot to be desired in terms of improved performance. On the other hand, model-based control design approaches such as \mathcal{H}_∞ -optimal control allow us to tune the system performance to a higher degree while giving better robustness to modeling uncertainties and disturbances[13].

In this thesis, we address the challenge of AFM control design by viewing the AFM from a systems perspective. Our approach to AFM control design mainly comprises firstly of investigating methods for characterizing the dynamical behavior of various AFM subsystems and the AFM system as a whole in the form of a dynamic system model. Subsequently, we apply advanced control theory tools to design and implement high-performance controllers for these models.

1.2.2 Hardware enhancements

Recent advances in nanopositioning hardware and reconfigurable computing devices are paving the way towards realizing the possibility of very high throughputs in AFM imaging. Almost all AFM systems in use today employ PID control designs. As a result, the speed of lateral scanning as a percentage of the resonance frequency of the cantilever probe is limited to under 1%. Innovations in nanopositioning stages have led to designs of lateral stages with bandwidths of more than 20 kHz and vertical stages with bandwidths in the range of a few hundred kHz. This means that lateral nanopositioning

stages have bandwidths as a percentage of the cantilever resonance frequency of 30-40% or even higher. To realize imaging at these higher speeds, cantilevers with very high resonance frequencies are being fabricated. However, high resonance frequency cantilevers tend to be very stiff and hence end up compromising on sensitivity. In order to take the best advantage of the improvements in lateral positioning bandwidths, we need the capability to design and implement model-based control designs that can push the limits of AFM imaging performance by order of magnitude while maintaining the high-resolution of imaging. Thanks to recent advances in reconfigurable computing devices, the capability to implement advanced model-based control designs is now possible on commercially available hardware.

Thus, to summarize our approach to improving AFM imaging, we apply recent hardware advances in conjunction with a systems-based viewpoint and use advanced control techniques. We discuss further on the scope of this thesis in the next section.

1.3 Scope of the thesis

The modes of operation of an Atomic Force Microscope can be broadly classified into static and dynamic modes. Dynamic modes of operation are preferred modes of operation for most practical applications due to a range of advantages they offer over static modes, which will be discussed further in chapter 2. Using the hardware capabilities built in our lab and a systems-based approach to design advanced control strategies, we investigated ways to further AFM scan speeds in dynamic operation.

First, this thesis proposes an improvement to an existing dynamic mode of imaging, known as Amplitude Modulation (AM-AFM) or tapping-mode imaging, by making use of an additional lower resolution sensor, the vertical position sensor, which is typically not used in the feedback loop. Using this additional sensor, we propose a cascaded control design that effectively cancels the effects of nonlinearities and resonance in the vertical positioning stage on imaging quality at higher speeds. We employ the robust loop-shaping control design method proposed in [14]. The robust control design provides up to 30% improvements in tapping-mode imaging.

Secondly, this thesis proposes a new dynamic imaging mode of operation for AFM by making use of a transform on the output signal. We improve further upon a solution for the design of linear model-based controllers, proposed earlier in our lab[15]. Instead of feeding back the cantilever deflection signal as proposed earlier, a transformed version of the deflection signal is used for feedback control. The output signal in existing imaging mode, i.e. the amplitude signal, in addition to being slow to change with respect to cantilever vibrations, also has a highly nonlinear relationship with respect to sample topography. This makes it challenging to design model-based controllers on conventional AM-AFM. We show that the signal obtained using the proposed transform, along-with an underlying model of AFM imaging for flat samples, exhibits a close to a linear relationship with the input signal. The transform has the effect of frequency shifting the output signal. We show the efficacy of the proposed transform-based method by implementing PID control and robust control designs for reference tracking. The motion of the actuator is shown to effectively reject the disturbance arising out of sample topography by simulating the proposed designs on a fully nonlinear model of the AFM system. The proposed control design achieves superior tracking performance at up to 6% of cantilever resonance frequency, which is a six times improvement over existing methods.

1.4 Organization of the thesis

This thesis is organized as follows. In chapter 2, we give a detailed description of Atomic Force Microscopy. In chapter 3, we discuss in detail some of the hardware advances that enable the feasibility of video-rate AFM imaging, including reconfigurable computing devices and nanopositioning stages, and also present some of the capabilities built in our lab. Based on these capabilities, we present solutions for enhancing AFM imaging bandwidth in Chapters 4 and 5. In chapter 4, we present a systems-based solution that enables the operation of an existing AFM imaging mode at up to 30% higher speeds. In chapter 5, we present a novel transform-based imaging mode to achieve an order of magnitude improvements in AFM imaging bandwidth. In chapter 6, we summarize the contributions of this thesis and discuss future research directions.

CHAPTER 2

ATOMIC FORCE MICROSCOPY

2.1 Historic Overview

The invention of the Scanning Tunneling Microscope (STM) and Atomic Force Microscope(AFM) are major milestones for nanoscience and nanotechnology research. Since the main sensing mechanism used to image samples is a microcantilever probe, these devices are commonly categorized as Scanning Probe Microscopes (SPMs). Over the years, these devices have facilitated the atomic-scale investigation of matter in an efficient, simple, and cost-effective manner. Prior to SPMs, resolutions of atomic-scale were possible using either electron microscopy or field-ion microscopy. However, these tools were complex and expensive. In 1981, Binnig and Rohrer invented the STM [16]. This contribution subsequently resulted in Binnig and Rohrer winning the 1986 Nobel Prize in Physics for inventing the STM. Since the principle of STM was based on regulating the tunneling current between the conducting cantilever probe tip and the sample, the utility of STM is limited to conducting samples. In 1986, the invention of AFM by Binnig, Quate, and Gerber made it possible to image non-conducting samples with atomic-scale resolution[1].

2.2 Principle of AFM

Atomic Force Microscopes rely on the ability to sense small atomic forces of interaction between the sample and the cantilever probe tip. The cantilever is designed to be insensitive to the disturbances from surrounding environments, such as building vibrations. These unwanted vibrations are typically below 2kHz. Thus the cantilever probes are designed to have resonance frequencies higher than 2kHz. The cantilever resonance frequency should not be

too high as a cantilever probe with high resonance frequency will have high stiffness, which reduces the sensitivity of the probe to tip-sample interaction forces. The cantilevers also need to be compliant in order to sense interatomic forces effectively. The tip-sample interaction forces are in the range of $10^{-7} - 10^{-12}$ Newtons. To produce a deflection greater than 1 Angstrom for a force of 10^{-12} N, the cantilever stiffness must be at most 0.01 N. AFM microcantilevers are typically made of silicon nitride or silicon oxide. Fig. 2.1 shows the schematic and working principle of a typical atomic force microscope. A laser beam is focussed onto the cantilever tip, which reflects from the top surface of the cantilever near the tip on to a split photodiode. Due to the deflection of the cantilever, the angle of reflection of the laser spot changes and hence the position of the spot on the photodiode changes. The photodiode outputs a voltage that corresponds to the position of the spot on the photodiode. Due to the longer length of the path of the laser spot, small changes in cantilever deflection get amplified by the photodiode. At the fixed end of the cantilever, also called the base of the cantilever, there is a dither piezo that provides a way to oscillate the base of the cantilever at the desired frequency. This feature is used in dynamic mode AFM imaging to vibrate the cantilever.

2.3 Imaging modes

The modes of operation of AFM for imaging can be broadly classified into two categories, static modes and dynamic modes. Static modes are the modes where the dither piezo is not used, i.e., the cantilever is not excited at its base. Dynamic modes are those where the cantilever is vibrated at a frequency near its resonance frequency by the dither piezo. Most commonly, AFM imaging is primarily done using either contact mode imaging or tapping mode imaging. Contact mode imaging is a static mode, and tapping mode is a dynamic mode. We provide a more detailed account of contact mode and tapping mode imaging below.

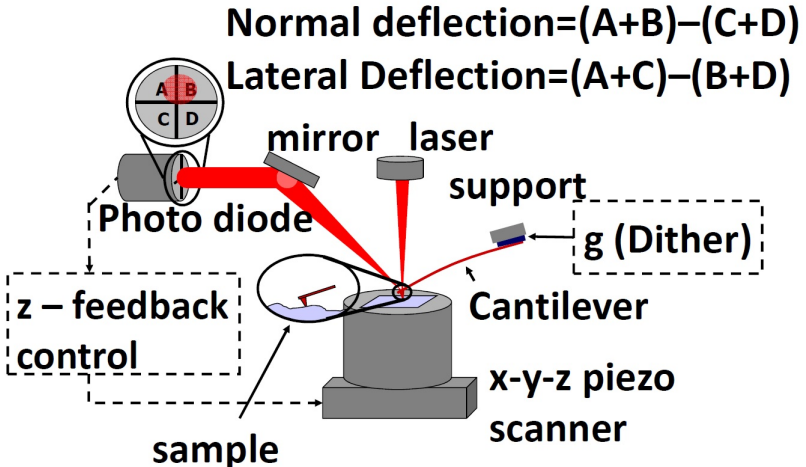


Figure 2.1: Schematic of an Atomic Force Microscope: The main probe in an Atomic Force is a microcantilever, which deflects due to forces between the atoms of the sample and the atoms of the tip. A laser incident on the tip reflects on to a photodiode, and this is used to sense the deflection of the sample. Depending on the mode of imaging, dither piezo actuator at the base of the cantilever can be used to vibrate the cantilever. An x-y-z piezo scanner positions the sample relative to the cantilever in the lateral and vertical directions

2.3.1 Contact mode imaging

Contact mode imaging is also referred to as constant-force mode. This is due to the fact that this mode uses the force balance principle. Fig. 2.2 shows a schematic of contact mode imaging operation. The sample is moved laterally in the x-y direction by the lateral scanning stage to cover the sample surface area of interest for imaging. Simultaneously, as the sample is moving laterally, the vertical positioning stage moves in the vertical direction to maintain a constant photodiode voltage. A PID controller is used on the vertical positioning stage where photodiode voltage is the signal to be regulated. As photodiode voltage is a measure of cantilever deflection, maintaining a fixed photodiode voltage is equivalent to maintaining a fixed cantilever deflection. In this mode, the vertical control signal gives a measure of the height of the topographic features on the sample. Since the dynamical model of the vertical piezo actuator is known, the vertical control signal can be used to derive the vertical piezo-actuator motion. Typically, within the bandwidth of operation of AFM imaging, the vertical piezo-actuator motion is simply a constant multiple of the input signal. The lateral coordinates of the feature

are given by sensors of the lateral positioning system. Thus, by plotting the vertical piezo-actuator displacement against the lateral x-y coordinates, we obtain an image of the sample topography. Contact mode imaging is very simple to implement, and the data is very easy to interpret. However, contact mode imaging is not suitable for soft samples due to tearing forces that arise between the tip and the sample. As a result, the cantilever could rip apart the sample. Soft samples like those typically used in biological applications need to be imaged using dynamic mode AFM operation.

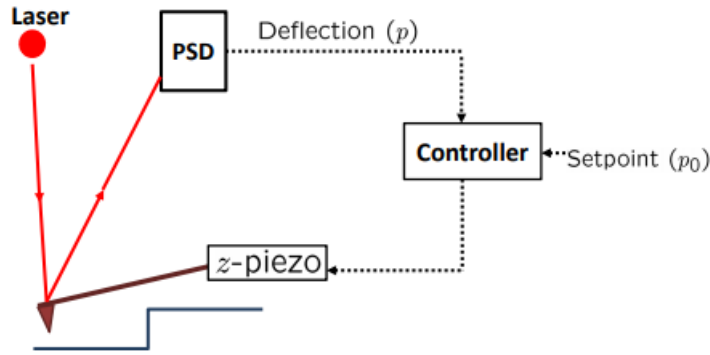


Figure 2.2: Contact mode imaging: The cantilever deflection signal is maintained at a constant set point value by actuating the vertical piezo-actuator. The control signal is used to estimate the sample topography

2.3.2 Tapping mode imaging

Tapping mode imaging, which is a dynamic mode of imaging, is also referred to as Amplitude Modulation imaging or AM-AFM. This is due to the fact that in this mode, the amplitude of the deflection of the cantilever is regulated. Fig. 2.3 shows a schematic of tapping mode imaging operation. The cantilever is excited by sinusoidally forcing the dither piezo at the first resonance frequency of the cantilever. As in contact mode imaging, the sample is moved laterally in the x-y direction by the lateral scanning stage to cover the sample surface area of interest for imaging. As the cantilever interacts with sample features, its amplitude of oscillation changes. The amplitude and phase of oscillation are obtained from the deflection signal by using a lock-in amplifier. Sometimes, peak detection is used to detect the amplitude of the

cantilever. The amplitude signal is used as the feedback signal. A PID controller regulates the amplitude to the desired setpoint amplitude by moving the vertical positioning stage. The vertical control signal is used to measure the height of the features on the sample. As in the case of contact-mode imaging, the image is constructed by plotting the vertical piezo-actuator displacement against the lateral x-y coordinates.

Advantages of dynamic mode imaging

Due to the nature of dynamic mode imaging, the cantilever tip contacts the sample only intermittently. This eliminates the problem of tearing forces that occur in contact mode imaging. Hence, dynamic modes are well suited for softer samples, including biosamples. Also, dynamic modes are robust for imaging in liquids. The amplitude of oscillation is typically in the range of 50-100 nm. Of this, the tip-sample interaction forces are significant in the 0-10 nm range. This also makes dynamic mode imaging more suitable for samples that have a large variation in sample features. A significant advantage of dynamic mode imaging is superior noise characteristics. Fig. 2.4 shows an experimentally obtained power spectral density plot of the response of the cantilever to thermal noise and a model fit for the cantilever dynamics [17]. It can be observed that the effects of thermal noise are more significant when compared to the effects of measurement noise near the resonance frequency of the cantilever. In the remaining areas, measurement noise dominates the effects of thermal noise. At a given ambient temperature, thermal noise limited resolution is the best that can be achieved. Hence, because dynamic imaging modes involve exciting the cantilever close to the resonance frequency, the measurement shows a high signal-to-noise ratio (SNR).

2.4 Cantilever Model

The first resonance mode of the cantilever is modeled as spring mass damper dynamics as follows.

$$\ddot{p} + \frac{\omega_n}{Q}\dot{p} + \omega_n^2 p = F(t), \quad (2.1)$$

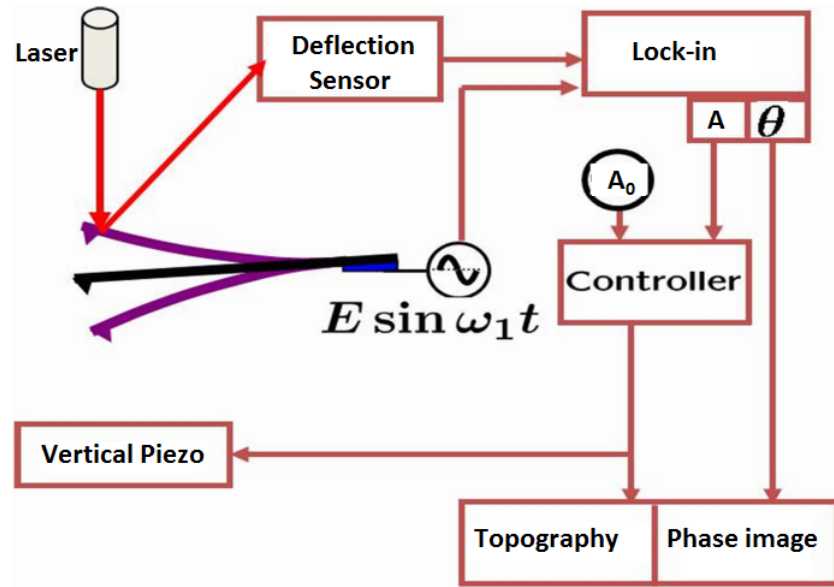


Figure 2.3: Tapping Mode imaging: The cantilever is excited at its first resonance frequency via a piezo at it's base. A lock-in Amplifier or sometimes a peak detector is used to infer the amplitude of the cantilever vibration. A controller is used to maintain the amplitude of cantilever vibration at a constant setpoint value A_0 by actuating the vertical piezo-actuator. The control signal is used to estimate the sample topography

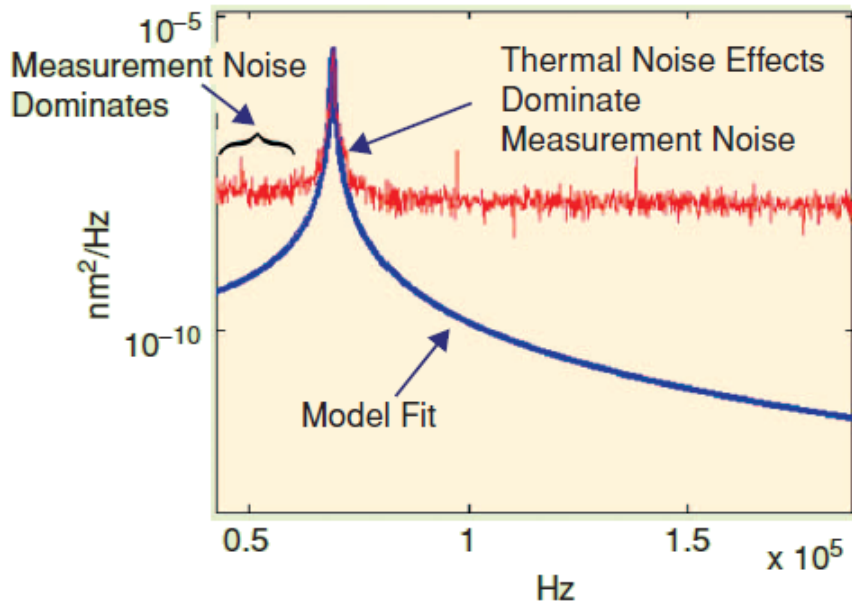


Figure 2.4: Effect of thermal noise on dynamic mode imaging. Near resonance frequency, the thermal noise response dominates the measurement noise.

where p is the deflection of the cantilever, ω_n is the first natural frequency of the cantilever, Q is the quality factor, and $F(t)$ is the forcing term. The quality factor characterizes the energy loss of the cantilever to the environment. Higher Q indicates a lower rate of energy loss and a low decay rate of oscillations. The resonance frequencies of typical AFM cantilevers are in the 2-400 kHz range. For high-speed tapping mode imaging, some of the cantilevers in use today have resonance frequencies higher than 1 MHz. The quality factor of the cantilever can be as low as 2 in liquids and as high as 10000 in vacuum.

2.4.1 Tip-sample interaction models

As the separation between the cantilever probe tip and the sample surface decreases when the cantilever approaches the surface of the sample, the cantilever starts experiencing forces due to the interactions between the atoms at the cantilever tip and the atoms of the sample surface. Fig.2.5 shows the typical variation of the tip-sample interaction force as a function of tip-sample separation. Short-range Van Der Waal forces act first, and these forces are

attractive forces that have the effect of pulling the cantilever tip towards the surface of the sample. As the separation further decreases, elastic forces arising out of the contact between the sample and the tip start acting. Ultimately beyond a minimum threshold of tip-sample separation, the forces are completely repulsive. Modeling of the tip-sample interaction is of very high importance in Atomic Force Microscopy and has been extensively studied. The force experienced by the cantilever is a combination of tip-sample interaction forces and also the compliance of the sample. To separate out these effects while imaging compliant samples, we need models for tip-sample interaction. A variety of models exist for the tip-sample separation. An appropriate model choice is made based on the type of the cantilever probe tip and the sample. For example, for tips with small curvature radius and high stiffness, the Derjaguin-Muller-Toropov (DMT) model[18] is applied. For tips with large curvature radius and low stiffness, the Johnson-Kendall-Roberts model[19] is more suitable.

2.4.2 Force Curves

Force curves are used to characterize the relationship between the tip-sample separation and the cantilever deflection. These curves are unique for every cantilever and hence are experimentally determined when a new cantilever is mounted for AFM imaging. The force curve is also used to obtain the parameter called Optical Lever Sensitivity (OLS) for the cantilever. OLS is the relationship between the photodiode voltage and the actual cantilever deflection in nanometers. Fig. 2.5 shows a typical experimental force curve.

2.5 Control of AFM imaging

The performance of the controller used in AFM imaging is vital for realizing high resolution and high bandwidth of imaging. To realize the goal of video-rate imaging, control strategies used will play an important role. Due to the complex nonlinearities in the tip-sample interaction forces, almost all the AFM imaging techniques in use today use PID controllers, which are not model-based. In this thesis, we utilize a systems approach to design model-based controllers for Atomic Force Microscopy. For this, we utilize the

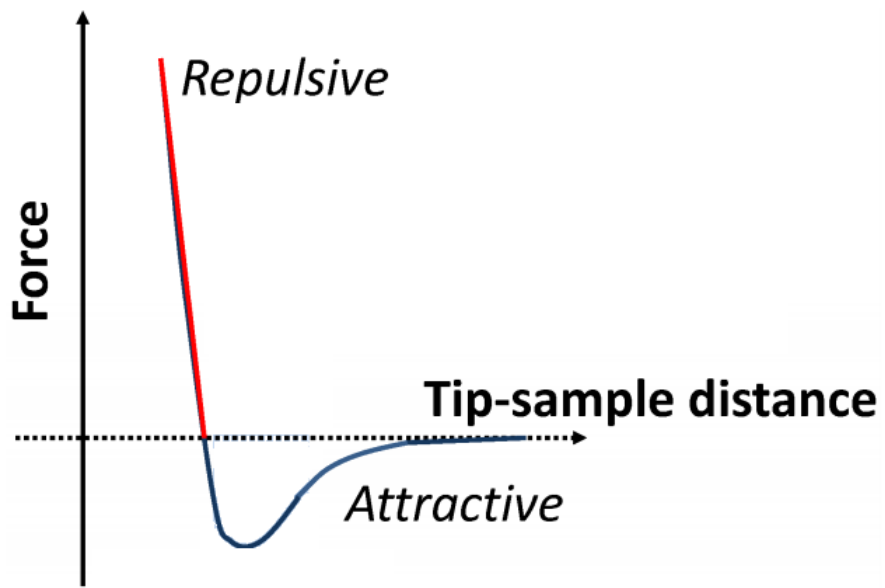


Figure 2.5: (a) Force curve showing the tip-sample interaction force as a function of distance. As the cantilever approaches the sample, it experiences attractive forces first (blue portion of the curve). As the tip comes closer, the forces are repulsive(red portion of the curve).

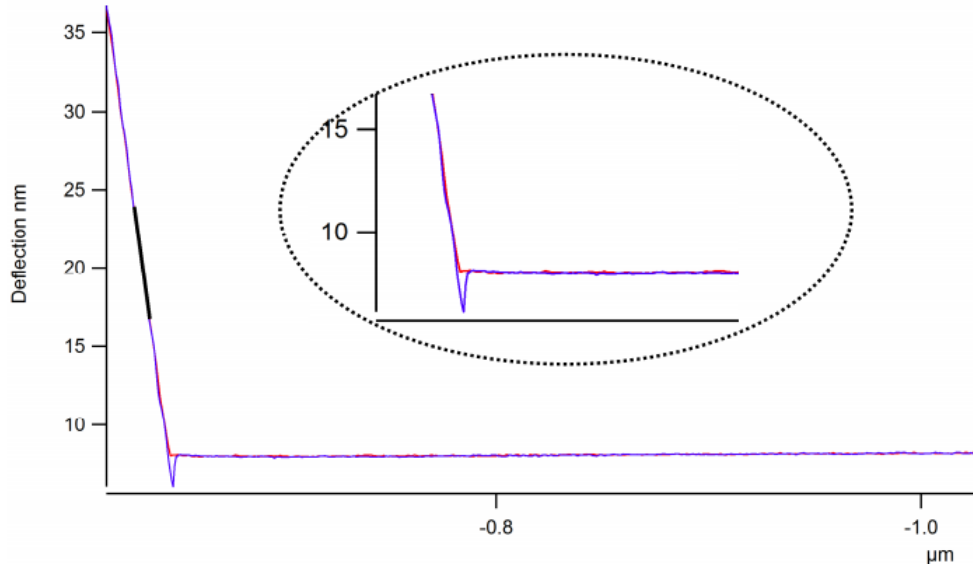


Figure 2.6: A typical experimental force curve that gives the relationship between cantilever deflection and tip-sample separation. The slope of the repulsive region is used to determine the Optical Lever Sensitivity (OLS)

knowledge of the models for cantilever dynamics and tip-sample interaction described in this chapter. The feasibility of these approaches is enabled by advances in AFM hardware, which we discuss in detail in the next chapter.

CHAPTER 3

ENABLING HARDWARE

The past decade saw a range of technological improvements in hardware used in AFMs. In this chapter, we present a comprehensive study of some of the key hardware advances that enable an order of magnitude improvements in the speed of AFM imaging. These advances can be classified broadly into two categories. Firstly, advances in hardware used to implement the control systems used for AFM imaging have opened up the possibility of implementing more advanced controllers, which were previously considered computationally complex for real-time implementation on previous generations of electronic devices. Secondly, advances in the mechanical design of lateral nanopositioning systems have led to these systems being capable of running at bandwidths an order of magnitude higher than what was possible earlier.

3.1 Electronics

Real-time computation is an essential aspect of AFM imaging. A well designed real-time computation solution is needed to process the information from various sensors and compute appropriate commands to be sent to various actuators, including the lateral and vertical nanopositioning stages. The history of real-time computation hardware for engineering applications has been traditionally dominated by Digital Signal Processors (DSPs). DSPs provide great flexibility in terms of software development for real-time implementation in a cost-effective manner. However, DSPs have a fixed computing architecture, that might limit their performance, especially in terms of the temporal processing bandwidth, for certain types of applications. On the other hand, application-specific fixed functionality hardware can be designed to give excellent performance efficiency but lack design flexibility offered by

DSPs.

In this context, reconfigurable computing devices offer a great mix of the flexibility of DSPs and the real-time performance efficiency of fixed-function hardware. The class of reconfigurable computing devices that gained the most attention during the 2000s was the Field Programmable Gate Arrays(FPGAs). FPGAs are a combination of programmable hardware logic blocks, and reconfigurable interconnects that allow the logic blocks to be connected as needed. The logic blocks, interconnects, and memory elements form the resources of the FPGA device. In addition to the hardware resources, another critical parameter that determines the capability of an FPGA device in terms of computing power is its clocking. With Moore’s law driving consistent shrinking of semiconductor device dimensions, the number of resources that can be packed onto FPGA devices has steadily increased. This has led to the availability of cost-effective, commercially available FPGA solutions that can be used to implement advanced control designs for AFM imaging.

In addition to FPGA hardware, in recent years, Field Programmable Analog Arrays (FPAA) are also being used for real-time computation solutions. Unlike FPGAs, which are comprised of digital blocks, FPAs provide analog blocks and interconnects for application design. They provide simple implementations using passive analog components such as opamps. This can be particularly useful for specific applications in atomic force microscopy. Some of the studies conducted in our lab using FPAA hardware are as follows.

3.1.1 Field Programmable Analog Arrays (FPAA) for AFM imaging

One of the major advantages of FPAA devices is that of implementing continuous-time controllers without having to discretize them as in the case of digital hardware

Tapping mode AFM imaging using FPAA to detect amplitude via peak detection

High-bandwidth detection of the amplitude of oscillation of an AFM cantilever is critical to achieving high-bandwidth tapping mode imaging. In existing tapping mode imaging, typically, a lock-in amplifier is used to de-

tect the amplitude of the cantilever deflection signal. The lock-in amplifier takes a few cycles to detect changes in amplitude. On the other hand, FPAs allow for peak-detection at very high speeds and thus allow us to measure changes in amplitude within one cycle, thus making the control algorithms faster when compared to a digital lock-in based implementation. In principle, peak detection can also be done digitally. However, for higher cantilever resonance frequencies, the sampling rate has to be very high in order to achieve accurate detection. Also, due to the sampling limitations and inherent nature of the detection method, the detection error increases with an increase in amplitude. This necessitates the electronics to support very high sampling rates as well as processing speeds. For cantilever resonance frequencies of the order of 300-400 kHz, this translates to very high demand on the speeds of the electronics. For this particular application, FPAs obviate the need for these high-speed electronics. The detection noise while using FPAs does not scale up with the amplitude, as in the case of digital implementation. We investigated Anadigm FPAs, which allow for amplitude detection by detecting the peak values of the deflection signal frequencies of up to 400kHz.

Fig. 3.1 shows the experimental results obtained by employing FPA based detection. We can see that FPA based peak detection detects amplitude changes faster than lock-in based detection on FPGA. To reject the high-frequency noise in FPA peak detection, we employ a low pass filter. The choice of corner frequency of the low-pass filter introduces a tradeoff between the speed of detection and noise elimination. Fig. 3.2 shows two cases with 10kHz and 100kHz corner frequencies respectively. Clearly, the first case with 10kHz corner frequency is less noisy but, at the same time, slower when compared to the second case with 100kHz corner frequency.

An FPA implementation of tapping mode imaging is shown in Fig. 3.3. The FPA block on the left is used for detecting amplitude. It consists of two peak detection blocks, one each to detect the highest and lowest values of the deflection signal, respectively. The deflection signal is prefiltered through a high-pass filter in order to filter any DC offset before peak detection. The difference between the highest peak value is then taken and passed through a low pass filter to get the amplitude signal after rejecting high-frequency noise. The FPA block on the right represents a PI controller used to regulate the amplitude signal to a set constant value.

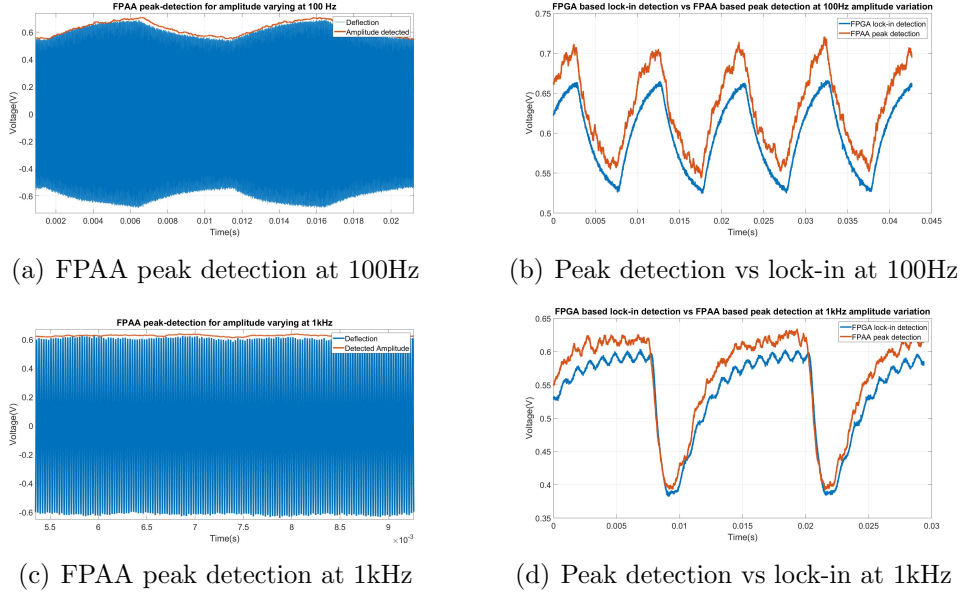


Figure 3.1: FPAA peak detection at 100Hz (top) and 1kHz(bottom).
Images on the left show cantilever deflection and amplitude detected using peak detection. Images on the right show a comparison between FPAA based peak detection and DSP based lock-in detection. The FPAA peak detection clearly leads the DSP lock-in based detection.

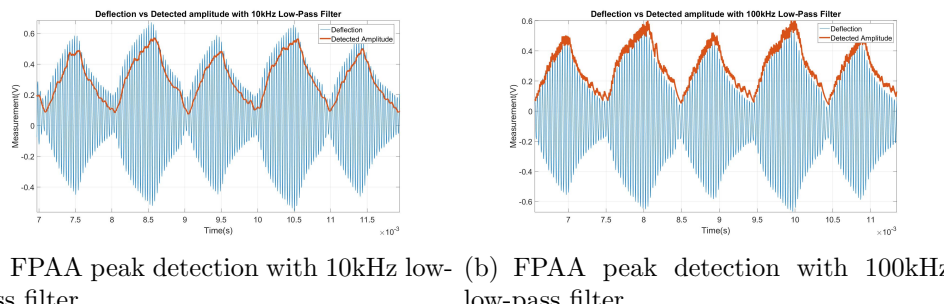


Figure 3.2: Noise-Speed tradeoff in FPAA peak detection: lower corner frequency of low pass filter (left) gives lower noise but slower detection

Fig. 3.4 shows a tapping mode image of a calibration grid, generated using peak detection.

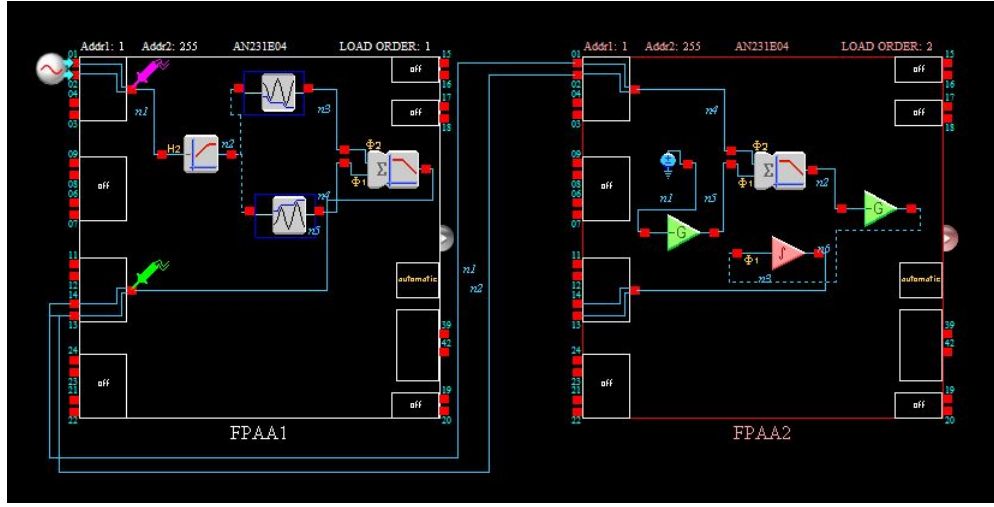


Figure 3.3: Tapping mode imaging: Amplitude detection and PID control

Contact Mode Imaging using FPAA

In contact mode imaging, the cantilever is regulated to exert a constant force on the sample by regulating the deflection value to a set constant. Fig. 3.5 shows the FPAA implementation of contact mode imaging, where the FPAA block is simply a PID controller with cantilever deflection signal as the input and vertical stage position as the output. Fig. 3.6 shows a contact mode image of a calibration grid, generated using this implementation.

3.1.2 FPGA technology

Though FPAA devices provide easy implementation of continuous-time transfer functions, multiple FPAA units need to be cascaded in order to implement a high order controller transfer function. In the past decade, FPGA devices with clock rates and computing hardware resources high enough to run advanced controllers that provide very high-bandwidths of hundreds of kHz have started becoming commercially available. This allows for the implementation of complex control designs in a single FPGA unit, thus eliminating the uncertainties such as noise that can arise from external cascading of FPAA

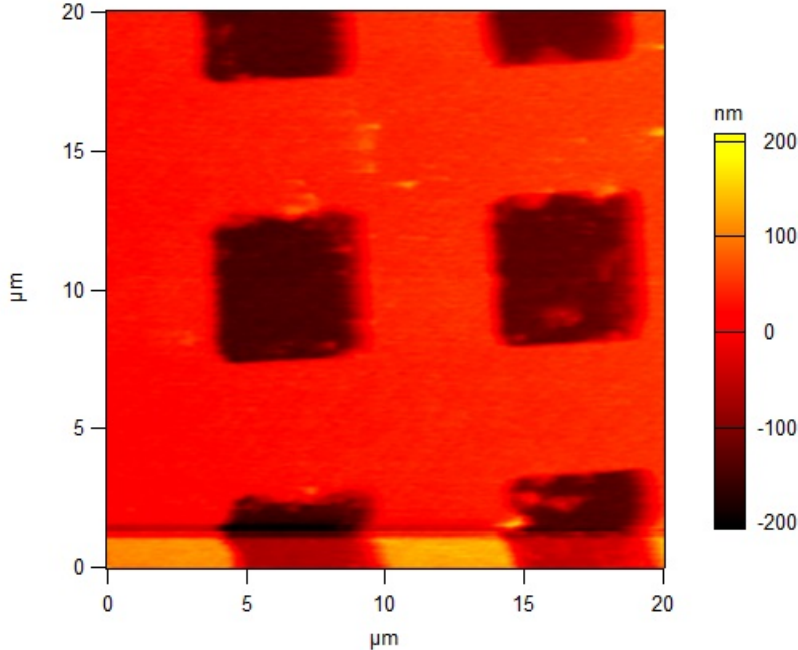


Figure 3.4: Tapping mode image of a calibration grid using peak detection

units. In addition, commercially available FPGA devices also facilitate one-stop programming solutions, thus offering further convenience in application development while offering better capabilities for real-time debugging and data-logging via user-friendly interfaces.

3.2 Nanopositioning stages

Nanopositioning forms one of the primary requirements of atomic force microscopy. As described in Chapter 2, during AFM imaging, the sample is scanned laterally with respect to the cantilever probe by the lateral nanopositioning stages. For accurate imaging, the nanopositioning system needs to have a high resolution. In addition, in order to achieve fast imaging, the nanopositioning system needs to have high bandwidth capability. Fundamentally, there are tradeoffs involved between the achievable resolution and the bandwidth of operation. In other words, achieving high bandwidth and high resolution at the same time is a challenging proposition. The tradeoffs between bandwidth and resolution are quantified in [20] and [21]. The bandwidth or speed of operation of the lateral nanopositioning stages was a

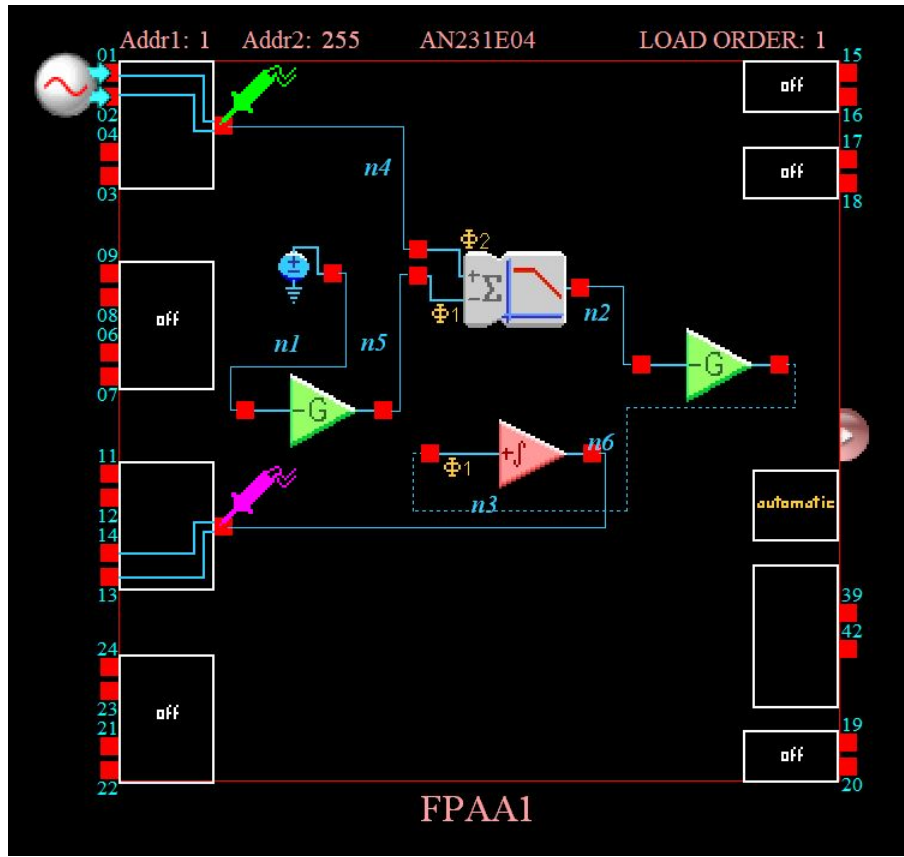


Figure 3.5: Contact mode imaging;PID control

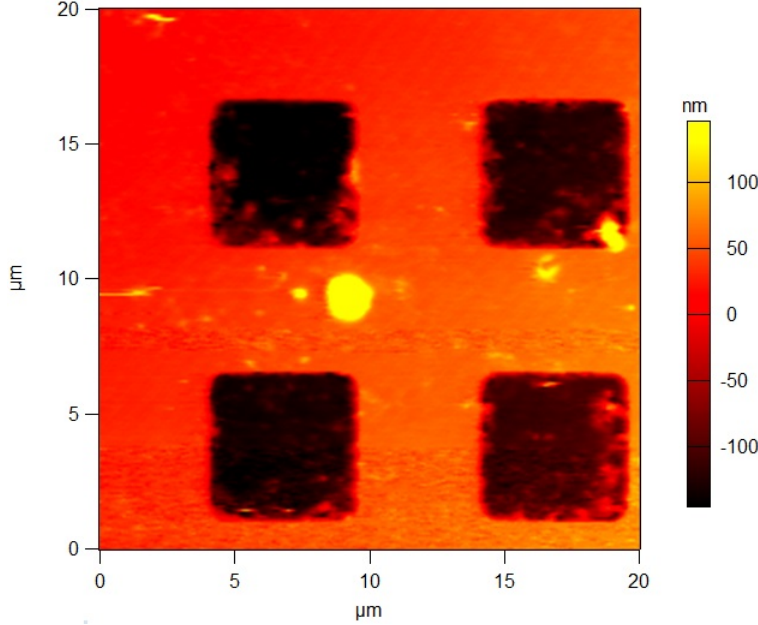


Figure 3.6: Contact mode imaging of a calibration grid using FPAA based control

limiting factor in terms of the speed of imaging in AFMs.

Another factor that limits the speed of AFM imaging is the bandwidth of the lateral nanopositioning system or the *XY*-stage. Earlier positioning stages had positioning bandwidths of under 1kHz. This translates to about 1% of the cantilever resonance frequency of most tapping mode cantilevers. The achievable bandwidths on nanopositioning stages are restrictions on the stage design. There has been considerable progress in the past decade in improving nanopositioning bandwidths. For example [22], [23], [24] and [25] demonstrate lateral stages with high positioning bandwidths. A recent design [26] achieves bandwidths higher than 20kHz, which represents an order of magnitude improvement over previous designs. This calls for the development of better AFM imaging methods, which give accurate sample topography estimation at these higher bandwidths.

With this background, we built hardware capabilities in our lab, which we describe in the next section.

3.3 Enhanced AFM setup

In order to facilitate the development of high-speed AFM imaging techniques, we have augmented several hardware solutions to our existing AFM setup.

3.3.1 High-bandwidth vertical nanopositioner

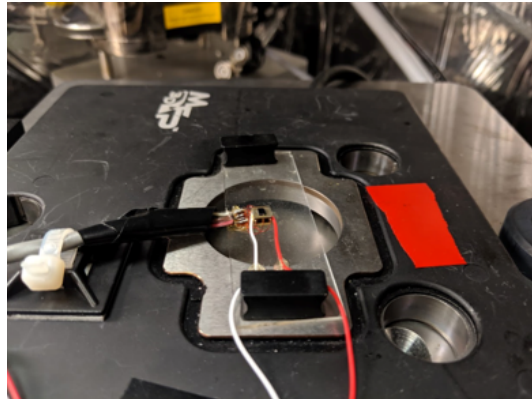
To enable high-bandwidth vertical positioning, we have integrated a custom-designed piezo actuator stage with a position sensor. Fig. 3.7 shows the details of this piezo actuator. The actuator has a first resonance frequency in the range of 250 kHz and hence is easily capable of providing vertical positioning bandwidth upwards of 100kHz.

3.3.2 NI FPGA hardware

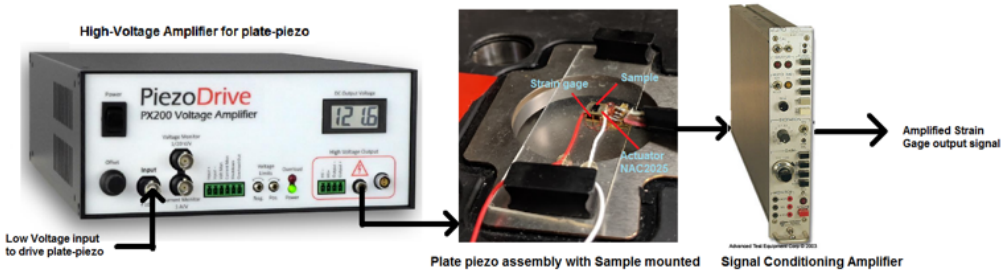
To implement high order control designs, we have incorporated a NI USB-7855R multifunction RIO device. This device is capable of a sampling rate of 1 MHz with an internal clock rate of 40 MHz. For implementing high order controller transfer functions, we employ a biquad implementation. We use the parallel computation capability of the FPGA device to cascade several biquad blocks. By overclocking the FPGA to 80MHz and parallelizing the controller computations, we are able to implement controllers of up to 14th order at about 480 kHz loop rate. In comparison, the earlier DSP in our lab was able to achieve loop rates of only 40-45 kHz.

3.4 Conclusion

In this chapter, we have presented on a variety of hardware solutions for enabling video-rate imaging. In particular, we can conclude that FPAs are more suitable for conventional AFM imaging. On the other hand, high-end FPGA based solutions provide ease of use for implementing complex controllers at high speeds. Using the knowledge gained from these studies, we have custom-selected hardware solutions and successfully integrated them into our existing lab setup. This has enabled us to perform studies on improving the speed of tapping mode AFM imaging using these hardware solutions



(a)



(b)

Figure 3.7: Custom designed plate-piezo based vertical nanopositioner hardware: (a) The AFM sample is stuck on to the vertical positioner. A strain gage is mounted on the sides of the nano positioner for accurate measurement of displacement. (b) The plate piezo element is driven by a high voltage amplifier that amplifies the input voltage 20 times. The signal from the strain gage is passed through a signal conditioning amplifier, which is set up to amplify the small strain gage signals by 2000 times.

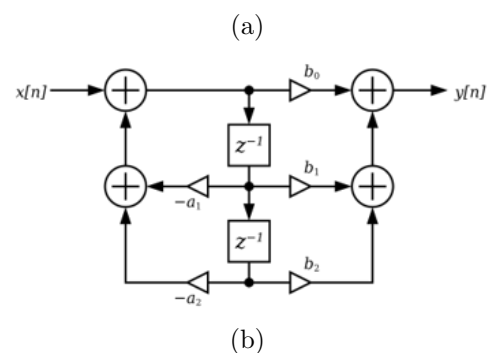


Figure 3.8: (a) NI USB 7855R for implementing advanced controllers (b) Direct form 2 implementation of biquad blocks with two delay elements

in combination with a comprehensive systems-based approach and advanced control design strategies. This work was primarily done using FPAAs hardware. Furthermore, we have also studied a new imaging mode, which gives advantages beyond tapping mode imaging. This work was primarily done using FPGA hardware in combination with a custom-designed high-bandwidth vertical positioning stage. We present these studies in the next two chapters.

CHAPTER 4

FAST TAPPING-MODE IMAGING USING MULTIPLE SENSORS

In this chapter, we provide a control design approach to enable tapping mode imaging at up to 30% faster speeds. The approach is based on a control redesign that aims at better reliability (robustness) of the piezo actuator, which translates into better bandwidth and robustness to uncertainties of the entire device. The central idea is to implement a cascaded control structure, with an inner control-loop and an outer control loop. The inner control-loop exploits the linear dynamical behavior of the vertical piezo-actuator and thus makes it possible for the outer-control loop to achieve higher bandwidth and robustness despite the uncertain and nonlinear dynamics of interaction between the AFM cantilever tip and the sample. The inner-loop control is facilitated by the vertical piezo-displacement (z -motion) sensor (also referred to as z -sensor). The z -sensor has a much lower bandwidth compared to the deflection sensor and is not used in typical existing designs. The linear dynamics of the inner plant (z -motion stage) allows for using advanced linear control approaches (such as \mathcal{H}_∞ framework) for rejecting nonlinear and high-frequency dynamics by treating them as disturbances. An interesting aspect of this design is that even though the z -sensor is a relatively low-resolution, low-bandwidth sensor (as opposed to a superior PSD based cantilever deflection sensor), the appropriate placement of this additional sensor in the overall control-scheme results in improved performance and robustness. This design is more effective in tapping mode AFM imaging, where severe challenges are imposed by the nonlinear relationship between the input to the piezo-actuator and the amplitude of the cantilever oscillations.

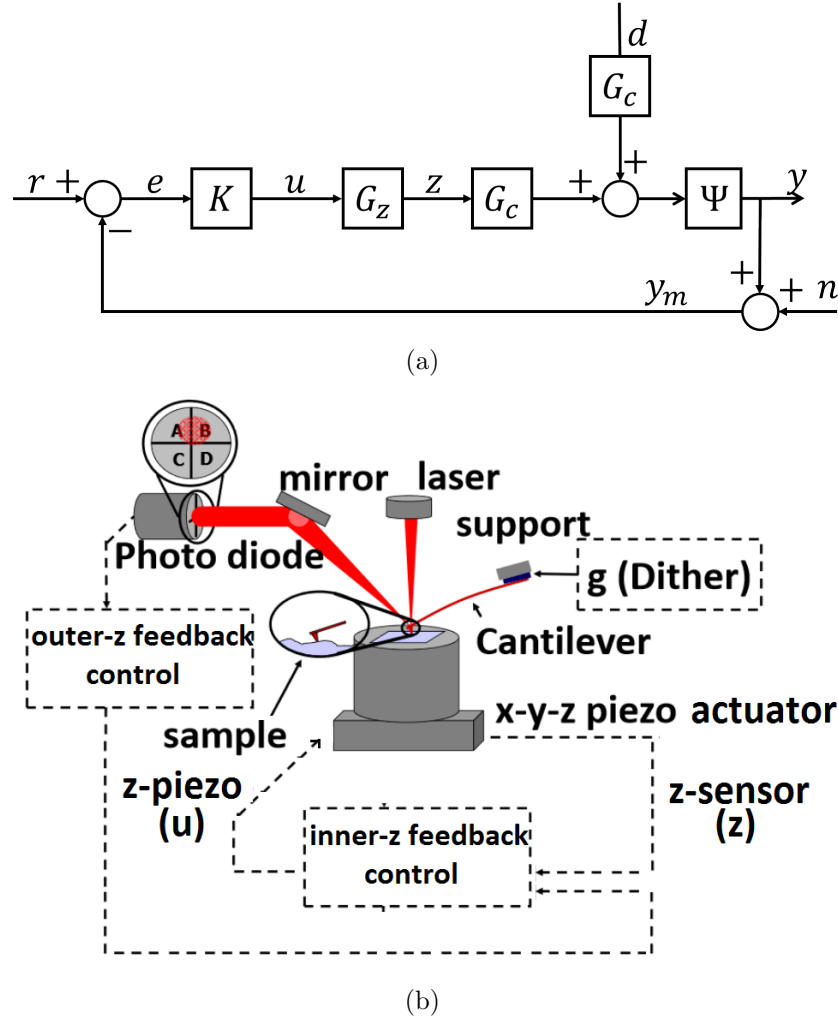


Figure 4.1: (a) Block diagram schematic for AFM imaging system with no z -sensor feedback. Here Ψ represents a functional block which is identity for contact-mode imaging and a non-linear amplitude-detection block for tapping-mode imaging. The reference signal, r is a deflection set-point for contact-mode imaging and amplitude set-point for tapping-mode imaging. Similarly, the measured output, y_m represents deflection of the cantilever tip for contact-mode imaging and amplitude of oscillation of the cantilever tip for tapping-mode operation. (b) Proposed control scheme with inner-outer control architecture. Notice that this scheme uses the z -sensor for inner-loop control contrary to conventional AFM control

4.1 Problem Formulation

We present our analysis and design in terms of transfer function block diagrams, as shown in Fig. 4.1(a). In this figure, G_z is the transfer function of the z -positioner comprising the actuator, flexure stage, and sensor. It represents a dynamical relationship between its output, the flexure stage displacement z , and its input, the voltage u given to the actuator (see Fig. 4.1(b)). Similarly, G_c represents the transfer function of the cantilever assembly comprising the tip-holder, dither actuator, and the PSD sensor. The signals d , n , and y represent disturbance due to sample-profile, the sensor noise, and the cantilever-tip deflection (in PSD voltage), respectively. The signals r and y_m represent the reference and the measured output, respectively (deflection for contact-mode, amplitude for tapping-mode). Ψ is a functional block that acts as an identity for contact-mode operation and as amplitude-detector for tapping-mode operation. K is the transfer function of the controller.

In the proposed approach, the inner- z controller is designed to attenuate the effects of high-frequency dynamics of the z -piezo actuator (particularly in tapping-mode), while the outer-controller is designed to achieve the overall reference tracking. We designed a feedback controller K_{fb} for the z -piezo actuator G_z that makes the tracking error small, attenuates effects of sensor noise, and is robust to modeling uncertainties (shown in Fig. 4.2). In [27], it is demonstrated in Fig. 10a that the frequency responses of a piezo actuator vary at different operating points. The variation in the responses is indicative of the modeling errors (uncertainties) in the identified plant. In addition, it is also observed that the frequency response at the same operating point varies when obtained at different times. In view of these uncertainties, the robustness of the closed-loop z -piezo actuator is a critical requirement of control design. We denote the closed-loop z -piezo actuator plant by \tilde{G}_z . The closed-loop plant \tilde{G}_z is shown in Fig. 4.2. Note that the deflection y_m has information on the piezo actuator motion z through the *nonlinear* tip-sample interaction Ψ , and sample profile d . Therefore, it is difficult for any control action that depends only on y_m to attenuate the effects of uncertainties in the piezo actuator. The piezo sensor motion z_m based control, on the other hand (shown in Fig. 4.2), is much better suited to address these effects.

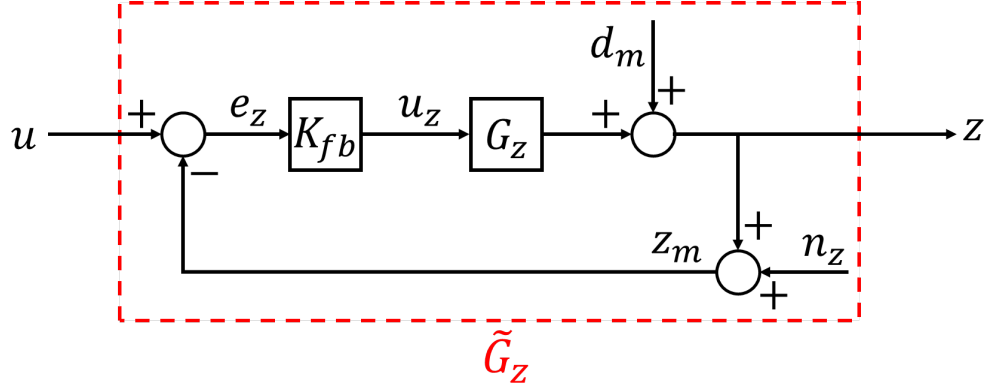


Figure 4.2: Block diagram schematic for the modified inner- z piezo actuator. Note that the proposed cascaded control scheme *replaces* the actual z -piezo actuator G_z (shown in Fig. 4.1(a)) with a suitably modified plant \tilde{G}_z that aims to mitigate the effects of uncertainties in piezo actuator motion. K_{fb} represents the transfer function for the inner-controller. Here, the signals u and z carry the same meanings as in Fig. 4.1(a). e_z is the error in tracking the commanded input u , while d_m represents the mechanical noise such as drift, creep, and hysteresis. n_z is the sensor-noise in the z -displacement measurement.

From this figure, we have,

$$\begin{aligned}
 \text{Tracking error, } e_z &= S(u - n_z), \\
 \text{Output displacement, } z &= G_z K_{fb} e_z = T(u - n_z), \\
 \text{Control input, } u_z &= K_{fb} e_z = K_{fb} S(u - n_z), \\
 S &= (1 + G_z K_{fb})^{-1}, \\
 \text{and, } T &= G_z K_{fb} (1 + G_z K_{fb})^{-1}, \tag{4.1}
 \end{aligned}$$

where, the sensitivity transfer function S is the closed-loop transfer function from reference u to tracking error e_z and measures the robustness of the closed-loop system to modeling and parametric plant uncertainties, and the complementary sensitivity transfer function T is the closed-loop transfer function from reference u to the displacement z (and from noise n_z to displacement z).

There are fundamental limitations on the achievable specifications, which, regardless of the control design, cannot be overcome [27], [28]. For instance, due to the algebraic constraint, $S + T = 1$, increasing the bandwidth of S would mean that T would still be large for relatively higher frequencies.

This, in turn, would result in significant amplification of high-frequency noise, thereby resulting in poor positioning resolution. The closed-loop transfer function $K_{fb}S$, which represents the dynamical relationship between e_z and the controller output u_z needs to be bounded, (since the maximum absolute drive voltage to piezo actuators in an AFM is bounded) in order to avoid effects such as saturation and equipment damage. In the context of piezo actuated stages, these conflicting objectives are addressed in an optimal, model-based configuration using a modern \mathcal{H}_∞ -control framework [27, 14, 29].

Having now discussed the various fundamental constraints with the inner-loop control design, it still remains unclear whether the improved inner-loop enhances the performance of the outer-loop. This becomes even more relevant in the case of AFMs, where the additional z -sensor is relatively inferior to the cantilever-tip displacement sensor in terms of resolution ($\sim 0.5\text{nm}$ average deviation for z -sensor compared to $< 0.02\text{nm}$ for photodiode sensor) and bandwidth ($\sim 10\text{kHz}$ for z -sensor compared to 2MHz for photodiode sensor). Fig. 4.3 shows the frequency response of the vertical z -piezo actuator in an MFP-3D AFM. The identification is performed using NI LabVIEW [30] and an NI PCIe-6361 DAQ card [31]. From the figure, one can observe sharp peaks at $\sim 1\text{kHz}$ and $\sim 2\text{kHz}$. This, in turn, implies that the output response of the z -piezo actuator gets amplified at these frequencies. Hence, if the z -piezo actuator is left uncontrolled, the effect of this high-frequency behavior gets propagated to other parts of the plant, thereby, resulting in spurious and unreliable imaging. In conventional AFM imaging, this problem is partially alleviated by designing low-bandwidth PI controllers with very small gains at high-frequencies, thus, restricting the bandwidth of the closed-loop system. The nonlinear dynamics of the plant, particularly in tapping-mode, which use only deflection measurements, make it difficult to design controllers for disturbance rejection at these frequencies. While the approach proposed in this work employs inner- z control to mitigate the effects of the high-frequency dynamics, *high-bandwidth* PI controllers are designed to control the outer-loop, thus, allowing faster scan rates.

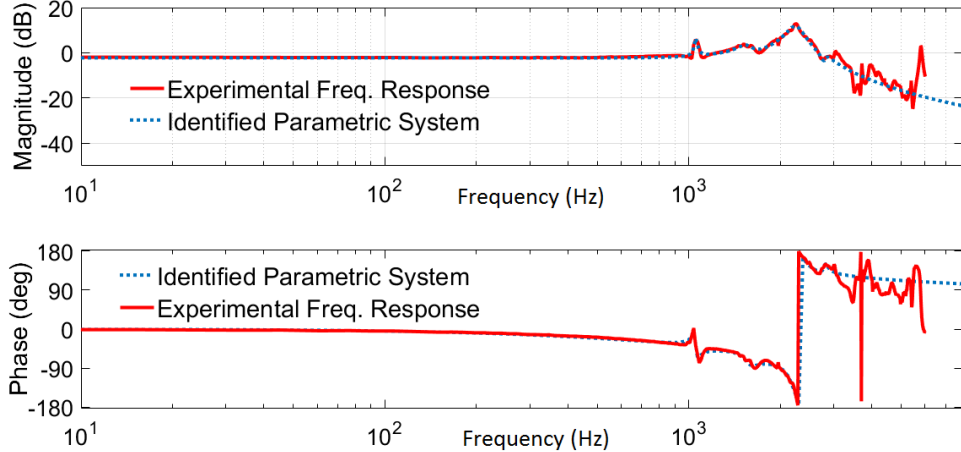


Figure 4.3: Experimental frequency response of the vertical z -piezo actuator in MFP-3D AFM and linear parametric fit to the experimental data in the operating frequency range.

4.2 Control design

The design of control laws for achieving *simultaneously* the above objectives renders tuning based control designs (PI/PII) impractical and ineffective. Therefore, we employ tools from the modern robust control-theoretic framework, where an optimal controller K over a set \mathcal{K} of proper, stabilizing controllers is sought by posing a feasible optimization problem for a given set of design specifications. The main advantage of this approach is that the performance objectives can be directly incorporated into the cost function. These optimization problems are of the form,

$$\min_{K \in \mathcal{K}} \|\Phi(K)\|_\infty \quad (4.2)$$

where, Φ is a matrix transfer function whose elements are in terms of the closed-loop transfer functions (such as in Eq. 4.1). For example, Φ represents a matrix transfer function from *external* variables, such as reference command and sensor noise, to *regulated* outputs, such as tracking error and control signal. In this case, minimizing $\|\Phi\|_\infty$ is equivalent to making the ratio of the magnitudes of regulated variables to external variables small, regardless of the external signals (i.e., the optimization problem seeks to minimize the worst-case gain from disturbance inputs to system outputs). These optimization problems have been studied extensively in [28], [32] and can

be solved efficiently using standard MATLAB routines. In this section, we present \mathcal{H}_∞ -control designs for the above goals using the *Glover-McFarlane robust loop-shaping approach* [33, 14].

Even though some piezo actuated positioning stages with pre-defined feedback controllers exhibit satisfactory resolution and tracking bandwidth at designed operating conditions, a slight deviation from these operating conditions may result in rapid degradation in tracking performance, sometimes resulting in system instability. This is indeed true with many flexure-based mechanisms which are very lowly damped and are close to being marginally stable. The Glover-McFarlane framework allows to first design controllers for high closed-loop bandwidth and later incorporate the robustness by characterizing the specific form of uncertainty. In [34], authors used Glover-McFarlane method [33, 14] to design control laws, which wrapped around pre-existing controllers, that resulted in significant improvements in robustness.

Fig. 4.4 shows the block-diagram for a Glover-McFarlane robust loop-shaping control design. In this framework, the given plant G_z is first pre-compensated using W_1 , so that the gain of the *shaped-plant*, $G_S = G_z W_1$ is sufficiently high at frequencies where good disturbance attenuation is required and is sufficiently low at frequencies where good robust stability is required. The robustness condition is imposed by requiring the controller to guarantee stability for a set of transfer function models that are ‘close’ to the nominal model G_S . The resulting optimal controller guarantees the stability of the closed-loop positioning system where the shaped-plant is represented by *any* transfer function G_p in the set:

$$\{G_p = (M - \Delta_M)^{-1}(N + \Delta_N), \|[\Delta_M \quad \Delta_N]\|_\infty \leq \gamma^{-1}\} \quad (4.3)$$

where, $G_S = M^{-1}N$ is a coprime factorization [35], $[\Delta_M \quad \Delta_N]$ represents the uncertain dynamics, and γ specifies a bound on this uncertainty. While the nominal shaped plant $G_S = M^{-1}N$ is deemed stable, the uncertainty set in Eq. 4.3 may still include plants that are marginally stable to even unstable. This characterization of uncertainty is particularly relevant to nanopositioning systems which typically have very low damping; uncertainties in plant parameters for such systems are well addressed by the uncertainty set in Eq. 4.3. Moreover, for a shaping controller K_S , the minimum possible γ can be

calculated *a priori*.

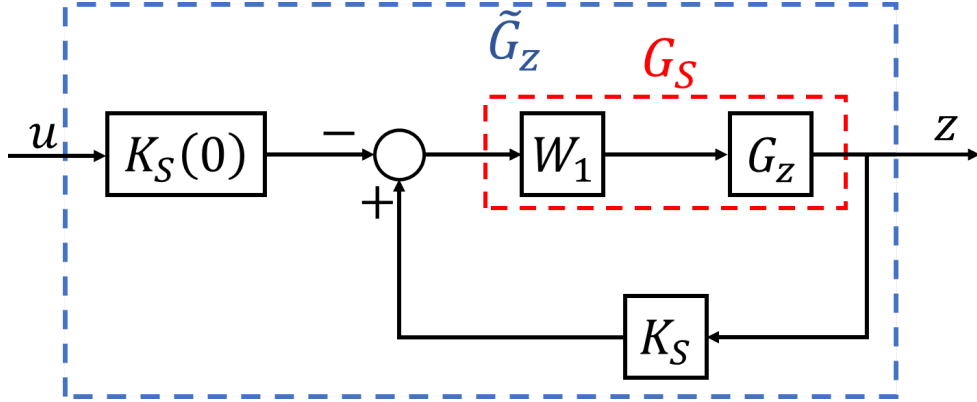


Figure 4.4: A Glover-McFarlane robust loop-shaping control framework with pre-compensator W_1

4.3 Inner-loop control using Glover-McFarlane robust loop-shaping

The frequency response of the vertical z -piezo actuator in our MFP-3D AFM is obtained using standard system identification methods, such as the black-box identification method [36]. A sine sweep signal, over a desired frequency range, is provided to the system and the z -sensor output is measured. A transfer function model is then fit to this experimental input-output data using MATLAB *invfreqs* command. Weighted iterative least square fitting was performed over 0 – 2kHz and the reduction through balanced realization [37] resulted in the following 9th-order parametric model (see Fig. 4.3):

$$G_z = \frac{-2683.3(s + 1.779 \times 10^4)(s - 2.261 \times 10^4)}{(s + 7242)(s^2 + 136.7s + 4.4 \times 10^7)} \\ \frac{(s^2 + 337.4s + 4.394 \times 10^7)(s^2 + 1689s + 1.006 \times 10^8)}{(s^2 + 1227s + 9.563 \times 10^7)(s^2 + 1729s + 1.999 \times 10^8)} \\ \frac{(s^2 + 578.2s + 3.083 \times 10^8)}{(s^2 + 748.9s + 3.119 \times 10^8)} \quad (4.4)$$

In conventional AFM imaging, in order to maintain a constant set-point (deflection/amplitude), typically an integral action is provided at the input of the z -piezo. In our approach for inner-loop control, the z -piezo actuator is first filtered through a modified PI precompensator W_1 . The precompensator

W_1 is chosen, so that the shaped-plant $G_S = G_z W_1$ has the desired integral action (high-gain at low-frequencies) and a small-gain near resonance frequency (but, not small enough to lower the bandwidth of the shaped-plant). The shaped-plant is then subjected to a closed-loop control using the Glover-McFarlane robust loop-shaping method [33, 14]. A remarkable feature of this design is that it achieves *robustness* with marginal reduction in performance. In fact, it is able to quantify the reduction by determining explicit bounds on how much it changes the loop gains at low and high frequencies. The precompensator W_1 was chosen to be $5000/(s + 10)$. The Glover-McFarlane design results in the following 9th-order controller. The resulting system ensures robustness with *gain-margin* of 9.92dB and *phase-margin* of 80.3°.

$$K_S = \frac{-1.5299(s + 7397)(s^2 + 68.32s + 4.349 \times 10^7)}{(s + 1.116 \times 10^4)(s^2 + 314.3s + 4.374 \times 10^7)} \\ \frac{(s^2 + 1114s + 9.417 \times 10^7)(s^2 + 320.3s + 1.967 \times 10^8)}{(s^2 + 1664s + 9.896 \times 10^7)(s^2 + 8209s + 2.928 \times 10^8)} \\ \frac{(s^2 + 752.8s + 3.12 \times 10^8)}{(s^2 + 749.5s + 3.095 \times 10^8)} \quad (4.5)$$

Fig. 4.5 shows the frequency response of the open-loop plant G_z and the closed-loop plant \tilde{G}_z . The closed-loop plant has a suppressed peak at the resonance frequency of the z -piezo actuator. Moreover, the closed-loop transfer function rolls-off faster without noticeable reduction in performance or bandwidth. A constant gain block is added during implementation to ensure 0dB steady-state gain. The controller is implemented using field programmable analog arrays (FPAs) [38], which have a direct bandwidth advantage over a very high-performance DSP [39].

Fig. 4.6 shows the experimental tracking response of the closed-loop system for a small-amplitude *noisy* 20Hz sinusoidal reference and a 500Hz (band-unlimited) triangular reference signals, respectively. While in Fig. 4.6(a), the closed-loop response is shown to be practically insensitive to signal *noise*, Fig. 4.6(b) demonstrates the efficacy of the control design in practical elimination of high-frequency component ($\sim 1.5\text{kHz}$) observed in the open-loop case. This is due to the flatter response of the closed-loop system when compared to the open-loop system as seen in Fig. 4.5.

Note: Fig. 4.7 shows the experimental noise spectrum of the z -sensor and follows the typical $1/f$ -noise (also known as Johnson noise). It is of-

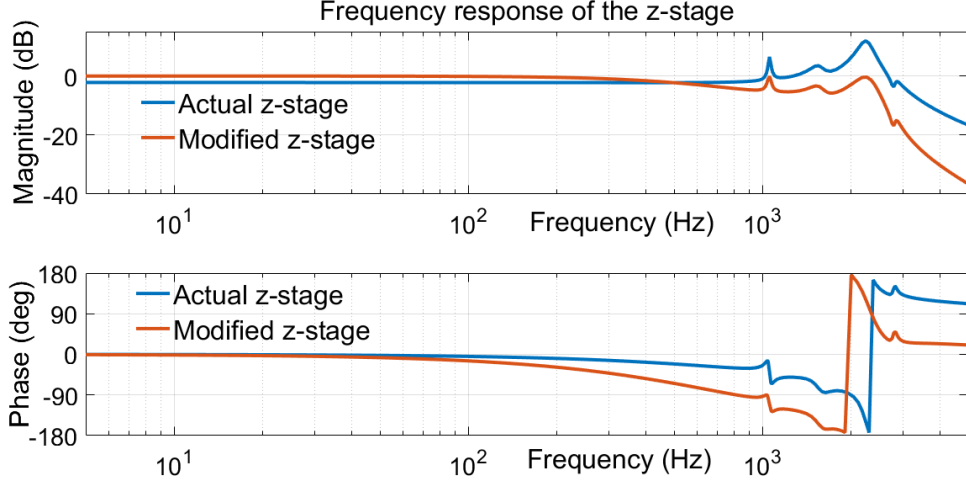


Figure 4.5: Bode-plots of the open-loop, and the closed-loop plants. The closed-loop system has small gain at the resonance frequency. Moreover, the closed-loop transfer function rolls-off faster at high-frequencies.

ten believed that incorporating an additional noisy sensor necessarily degrades the performance of the overall system. While this may be true for certain systems whose exact parametric models are available, this is certainly not the case with most piezo-based systems. Let us denote the effects of uncertainties in dynamics of the z -piezo actuator as *mechanical noise*. The proposed feedback-based approach allows a trade-off between mechanical and sensor noise. Moreover, a large separation between the resonance frequencies of the cantilever (ω_c) and the z -piezo (ω_z) ensures that the effect of z -sensor noise on the cantilever deflection is practically negligible. This can be understood as follows. For ‘acceptable’ topography measurement, it is required that the lateral bandwidth ω_l (proportional to the number of sample features per unit time) is smaller than the vertical (z) positioning bandwidth ω_z . Without loss of generality, let us assume that the amplitude of the deflection signal at time t due to variation in sample profile is given by $A(t) = \cos(\omega_l t)$, while the cantilever oscillates at its resonance frequency ω_c . Thus, the cantilever deflection is approximately (disregarding minor variations in resonance frequency due to tip-sample interaction) given by $y(t) = \cos(\omega_l t) \cos(\omega_c t + \phi) = \cos((\omega_c + \omega_l)t + \phi) + \cos((\omega_c - \omega_l)t + \phi)$, where ϕ is the steady-state phase difference due to tip-sample interaction. Since $\omega_c \gg \omega_l$ and the sensor noise is inversely proportional to the frequency, the effect of noise at frequencies $(\omega_c + \omega_l)$ and $(\omega_c - \omega_l)$ is practically negligible.

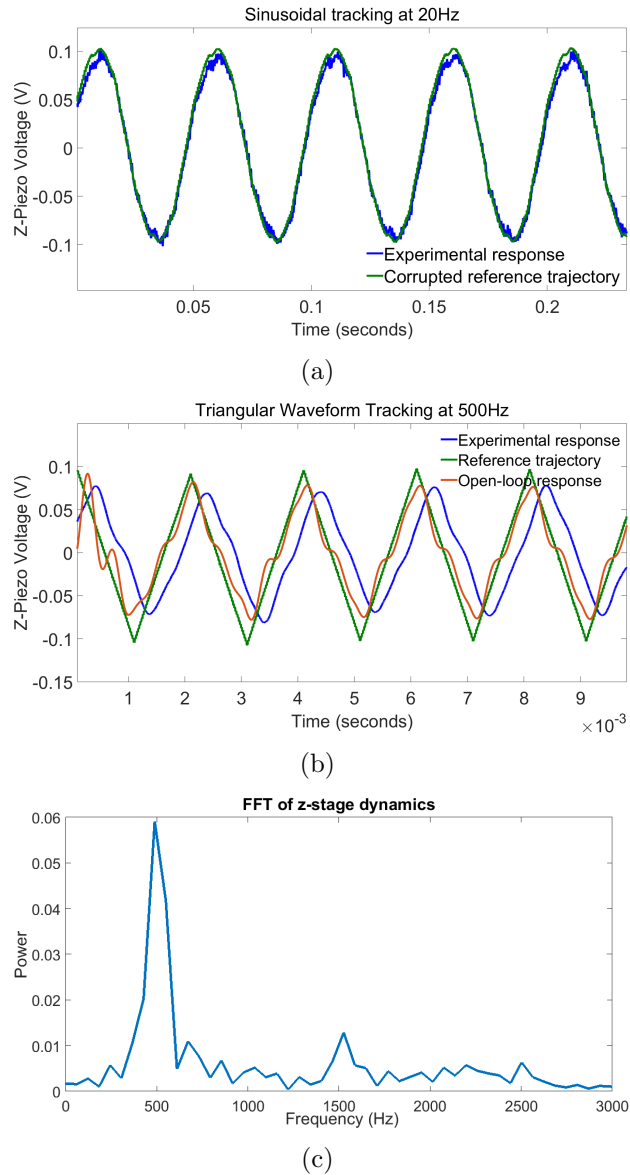


Figure 4.6: Experimental tracking response of the FPAA based implementation of Glover-McFarlane robust loop-shaping control design for the vertical z -piezo actuator. (a) Tracking response to *noisy* 20Hz sinusoidal signal. The tracking response is practically insensitive to signal noise, i.e., the effect of z -sensor noise is imperceptible (compared to the original signal). (b) Open-loop and closed-loop response to 500Hz triangular signal. It can be seen that there is a high-frequency (1.5kHz) signal riding on the 500Hz component for the open-loop response, which in turn shows the effect of the high-frequency dynamics. Since, the z -sensor output is used as a measurement signal for topography estimation in AFM imaging, the high-frequency behavior results in spurious image construction. (c) FFT of the output response of open-loop plant.

This is corroborated by our experiments too, as we did not observe any visual change in the deflection sensor noise with and without the inner-loop control.

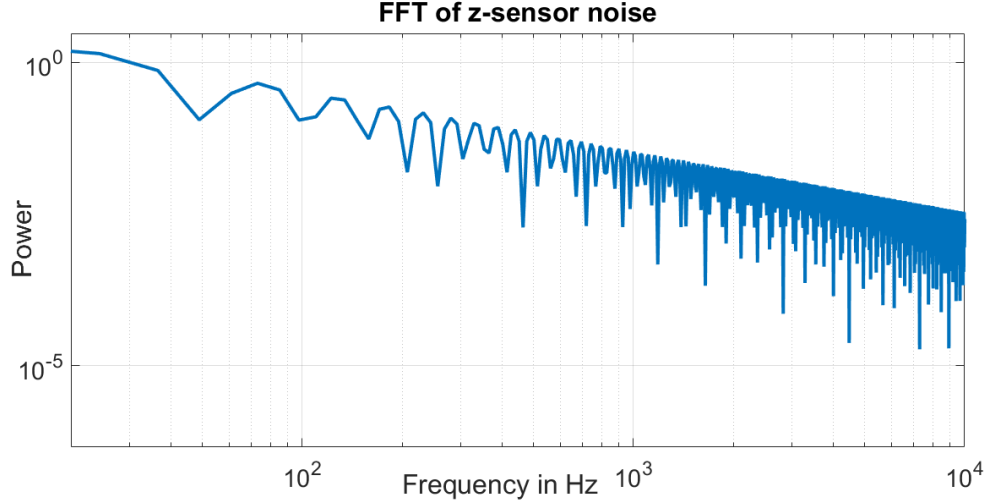


Figure 4.7: Power spectrum of z -sensor noise. As expected, the sensor noise follows the well-known Johnson noise ($1/f$ noise).

4.4 Outer-loop control for amplitude regulation in tapping-mode imaging

In tapping-mode imaging, an outer-loop controller maintains a constant amplitude set-point by regulating the displacement of the z -piezo actuator (without any inner control). The choice of outer-loop control is limited to PI (or its variant), primarily due to the complex and uncertain cantilever amplitude dynamic models. However, from Fig. 4.5, it is evident that in the absence of inner- z control, one has to contend with low-bandwidth imaging (closed-loop control) in order to avoid the effects of the high-frequency dynamics of the z -piezo actuator. The effect can be observed in the open-loop response of the z -piezo actuator for a 500Hz triangular input signal (see Fig. 4.6(b)), where a high-frequency behavior sits atop the 500Hz component. The associated nonlinearities with amplitude dynamics make it difficult to estimate the effects of the high-frequency dynamics and thus, these effects can not be separated from the true topography measurements. Hence, a high-bandwidth

outer-loop control with no inner-control leads to spurious imaging results, due to the unsuppressed high-frequency z dynamics.

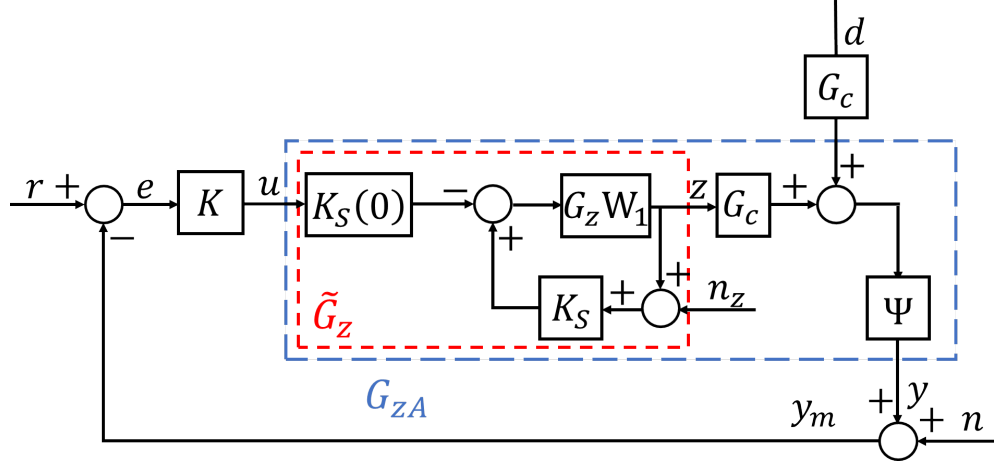


Figure 4.8: Block diagram representation of control scheme for tapping-mode imaging.

Fig. 4.8 shows the block diagram for the proposed *inner-outer* control framework for tapping-mode imaging. The inner-controlled loop is denoted by \tilde{G}_z . For outer-control design, we treat G_{zA} , the transfer function from output u of the controller to amplitude y , as a plant and design controller K so that the amplitude y is regulated at a constant r . Note that the plant G_{zA} described in this context is nonlinear and exhibits different dynamical behavior at different operating points. Fig. 4.9 shows the experimental frequency response of the plant G_{zA} for the two cases - (a) no inner-loop control: As evident from the Fig. 4.9(a), there is an abrupt change in the system gain at frequencies ($\sim 1\text{kHz}$) and ($\sim 2\text{kHz}$); moreover, the effect of the high-frequency behavior is unpredictable for different amplitude set-points and in-air drive amplitudes (b) with inner-loop control: With the proposed Glover-McFarlane controller with the appropriately chosen precompensator, the effect of high-frequency dynamics becomes virtually non-existent. For this experiment, we used AC240TS cantilever probe [40] with a nominal resonance frequency of 76kHz and nominal spring constant 2N/m.

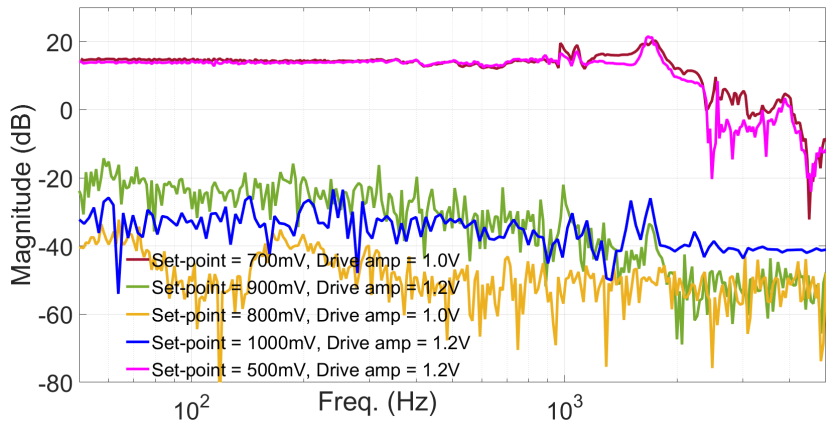
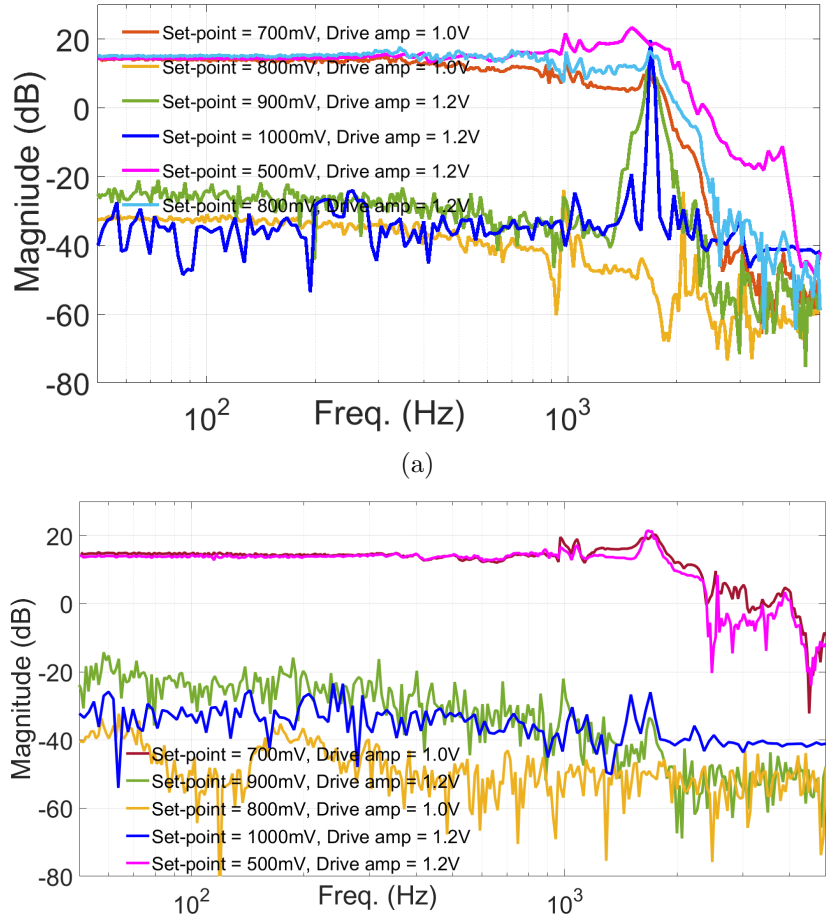


Figure 4.9: Experimental frequency response for the plant G_{zA} with (a) *no inner-loop control* - effect of high-frequency dynamics is both noticeable and unpredictable, (b) *Glover-McFarlane controller for the inner-loop* - effect of high-frequency dynamics is virtually non-existent. The frequency response plot with large magnitude values suggest *hard* engagement between the tip and the sample, whereas the low magnitude values are the results of *soft* engagement

4.5 Experimental Results

We now investigate the effect of inner- z control for designing the outer-loop controller. In tapping-mode imaging, nonlinear amplitude dynamics prevent the use of linear model-based controllers for the outer-loop. We, therefore, restrict ourselves to designing integral controllers for the outer-loop. Moreover, the plant dynamics changes with variations in amplitude set-points and cantilever drive amplitudes (due to associated nonlinearities in tip-sample interactions). Hence for both the cases (i.e., with or without inner-loop control), we first design outer controllers for the plants that depict *hard* engagement between the cantilever-tip and the sample represented by the set-point (s.p.) = 500mV and drive-amplitude (d.a.) = 1.2V, and employ the same control laws to study the cases where the cantilever is softly engaged to the sample represented by the set-point (s.p.) = 900mV and drive-amplitude (d.a.) = 1.2V. For the sake of fair comparisons in robustness, exhaustively tuned integral outer-controllers are tested to achieve similar bandwidths (~ 200 Hz) for the scenario of hard-engagement and for the two cases - (1) *No control on z-piezo actuator* - the optimal integral controller is obtained as $K_1 = \frac{500}{s}$, (2) *Glover-McFarlane control on z-piezo actuator* - the resulting integral controller is obtained as $K_2 = \frac{395}{s}$.

Fig. 4.10(a) shows the experimental and simulation closed-loop responses for the conventional (no inner-loop control) and the proposed (with inner-loop control) approach for the hard-engagement scenario. The experimental and simulation responses corroborate the usefulness of the proposed inner-outer control design. In the conventional tapping-mode imaging with no inner-loop control, the overall set-point to amplitude dynamics is adversely affected at the resonance frequency of the z -piezo actuator, which is seen clearly in the experimental closed-loop complementary sensitivity transfer function in Fig. 4.10(a). This is also observed in Fig. 4.10(b) for the proposed design, where the peak in the sensitivity plot is practically eliminated, thereby allowing a very high gain margin and making the design practically insensitive to modeling uncertainties. The controllers K_1 and K_2 are then tested for the scenario where the cantilever-tip is softly engaged to the sample (see Fig. 4.11). Note that in this scenario, the controller results in relatively much smaller closed-loop bandwidths as the system gains are very small in the frequencies of operation. However, a small peak near the resonance fre-

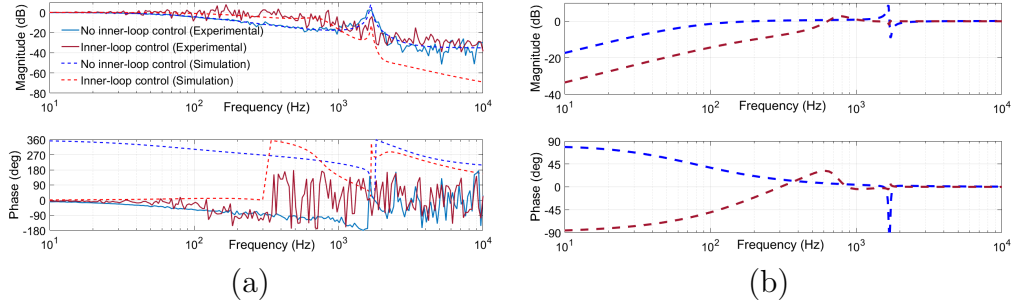


Figure 4.10: Closed-loop frequency responses for the case of hard-engagement. (a) Experimental and Simulated complementary sensitivity transfer functions - In the conventional tapping-mode imaging with no inner-loop control, the overall set-point to amplitude dynamics is adversely affected at the resonance frequency of the z -piezo actuator. (b) Simulated sensitivity transfer functions - The sensitivity peak is practically eliminated for the proposed design.

quency of the z -piezo actuator in the sensitivity plot (see Fig. 4.11(b)) is still observed for the plant with no inner-control, thereby indicating slightly poor robustness around those frequencies.

Remark: Note that the proposed inner-outer control scheme does not have any significant advantage over the conventional control scheme for the scenarios that capture excessively soft engagements between the cantilever-tip and the sample (shown by orange curve in Fig. 4.9(a)). This is primarily due to very small frequency-response gains (see Fig. 4.9(a)), resulting in closed-loop transfer functions that die off much below the resonance frequency of the z -piezo actuator. However, the proposed approach still outscores the conventional approach for moderately soft engagements (as shown in Fig. 4.11). Thus the proposed design is particularly useful for scenarios that correspond to hard to moderately soft engagement between the tip and the sample. However, it should be remarked that any practical imaging will require sufficiently hard engagement between the tip and the sample.

Application of the proposed approach for contact-mode imaging: A similar comparison exists for contact-mode AFM imaging with PI controller for the outer loop, as is the case with usual contact-mode imaging. We used contact-mode silicon probe [41] with resonance frequency $\sim 13\text{kHz}$. Exhaustively tuned PI controllers are derived using MATLAB/Simulink for the two

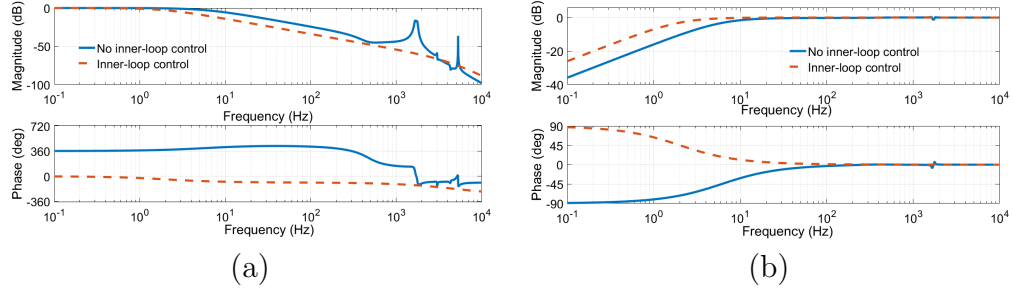


Figure 4.11: Closed-loop transfer functions for the case of soft-engagement.
(a)Complementary sensitivity transfer functions - The effect of the z -piezo actuator dynamics is clearly seen in the uncontrolled z inner-loop case.
(b)Sensitivity transfer functions - There is no observable sensitivity peak for the proposed approach.

cases - (1) *No control on z-piezo actuator* - the PID tuner block resulted in the following optimal PI controller, $K = \frac{1902.27}{s}$. The resulting closed-loop bandwidth was 234Hz, with a peak sensitivity value of 4.34dB. (2) *Glover-McFarlane control on z-piezo actuator* - the optimal control law in this case was $K = 0.102 + \frac{2068}{s}$. The resulting closed-loop bandwidth and peak sensitivity values were 315Hz and 3.37dB, respectively. Thus, a 34.79% improvement in tracking bandwidth and a 22.35% decrease in peak sensitivity values (a measure for robustness [28, 17]) were obtained with the modified z -plant. Fig. 4.12 shows the closed-loop sensitivity and complementary sensitivity transfer functions for the two cases.

However, we must specify that it is still possible to achieve comparable performance and robustness for contact-mode imaging without the need for additional z -control, as shown in [42]. This is mainly due to the availability of linear plant models and a wide separation in the resonance frequencies of the contact-mode cantilever and the vertical z -piezo actuator. Modern \mathcal{H}_∞ based outer-controllers are designed in [42] to eliminate the effects of high-frequency dynamics of the z -piezo actuator without having to include additional z -sensor in the overall control scheme.

Tapping-mode AFM imaging using the proposed inner-outer design and comparisons with the usual tapping-mode: We now discuss the advantages of the proposed modified z -piezo actuator for AFM imaging. As discussed earlier, the proposed design renders the closed-loop imaging system *insensitive* to small variations in set-points and scanning speeds as compared to the usual

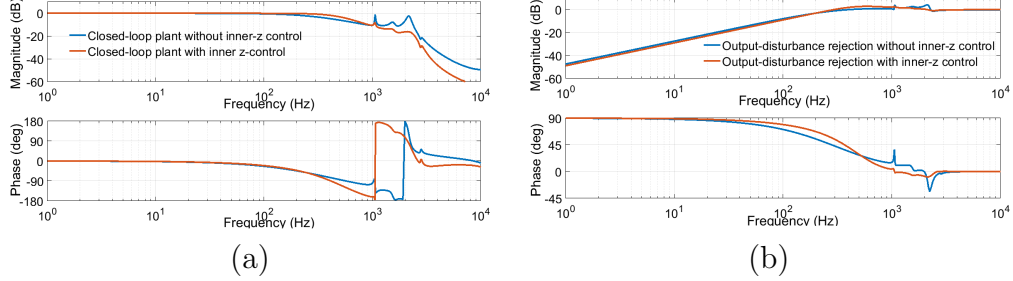


Figure 4.12: Complementary sensitivity and sensitivity transfer functions for the closed-loop control of contact-mode imaging. (a) The complementary sensitivity plot for the controlled inner-loop (red) rolls-off faster at high frequencies; moreover, the achievable bandwidth is higher than in the case of uncontrolled z -piezo actuator (blue). (b) The sensitivity plot for the controlled inner-loop case (red) lies below the sensitivity plot for the uncontrolled z -piezo actuator case (blue) for frequencies below the crossover frequency. Moreover, there is a sharp peak near the resonance frequency of the z -piezo actuator in the latter case, thereby degrading robustness at those frequencies.

tapping-mode imaging where the z -piezo actuator is left uncontrolled. The effects of the proposed design are reflected in AFM images through *sharpness* of features and *improved* trace-retrace characteristics. A calibration grating with $5\mu\text{m} \times 5\mu\text{m}$ pitch and 25nm feature height is considered for experimental comparison of the two approaches. The outer controllers are tuned exhaustively for the two scenarios (with and without inner-loop control) and the scans are obtained at varying set points and scanning speeds.

Fig. 4.13 shows section (line) scans of the calibration grating along the x -direction at a set-point of 800mV and scan-speed of 20Hz . Clearly the proposed approach results in better estimates of the feature heights (25nm), whereas the usual tapping-mode images of the *same* feature provide *inaccurate* information about the feature dimensions ($\sim 30\text{nm}$). Moreover, the feature reconstruction is relatively *sharper* in the case of tapping-mode imaging with inner-loop control (see Fig. 4.13c).

As stated earlier, the outer PI controllers for the two scenarios - with and without inner-loop control, are tuned for comparable performances at a nominal set-point of 600mV and a scan-speed of 20Hz . This is reflected in the excellent trace-retrace characteristics along the x -direction (as shown in Figs. 4.14a,d). While the feature heights and shapes, and trace-retrace plots are

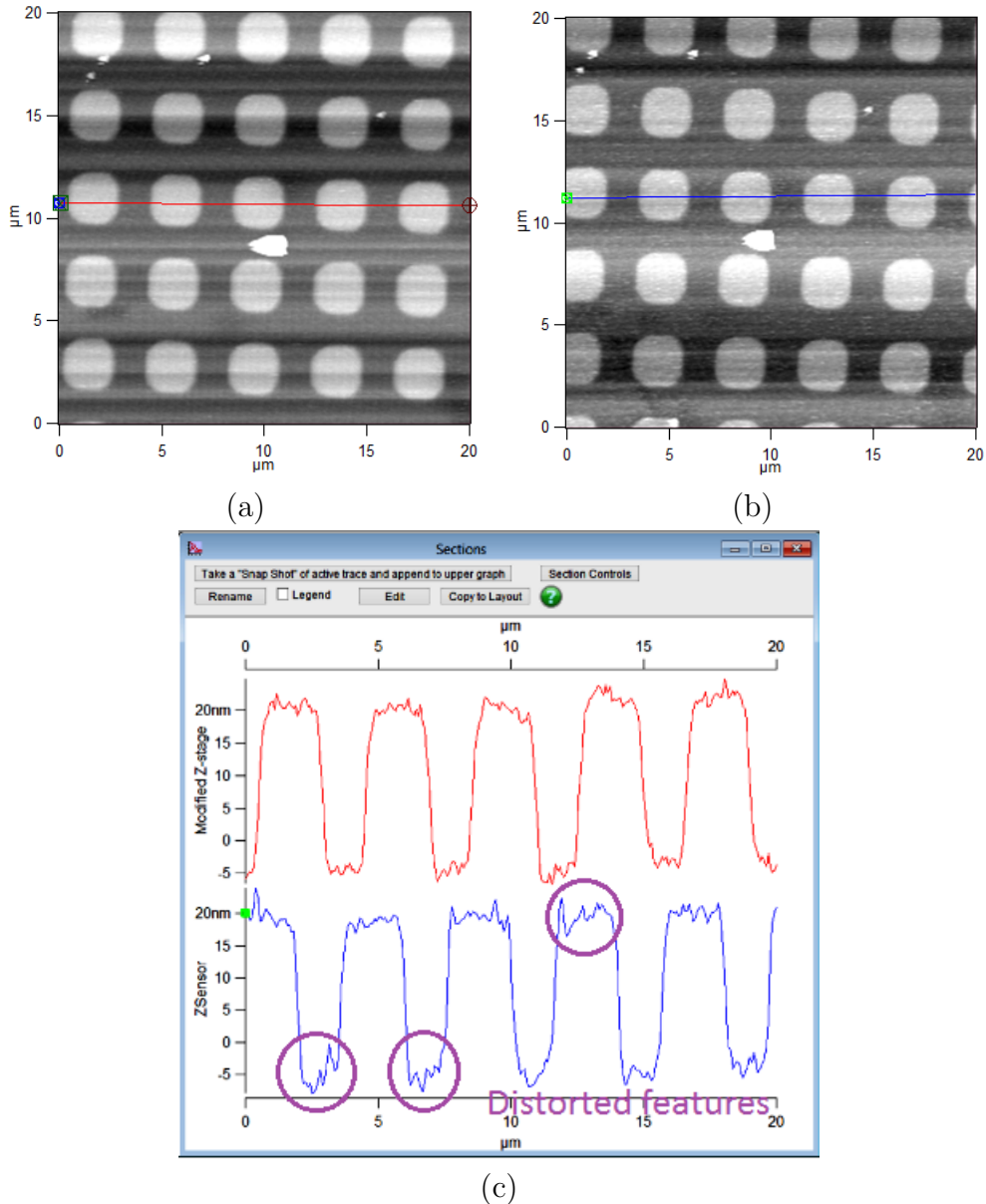


Figure 4.13: Section scans of a calibration grating using (a) the proposed modified z -piezo actuator control, (b) without inner-loop control. (c) The proposed approach provides better estimates of the feature dimensions with sharper profile.

indistinguishable for a low-speed scan, the proposed control design with an inner-loop control on the z -piezo actuator results in improved performance for faster scan - 100Hz (see Figs. 4.14b,e) with sharper borders. The region of interest in the calibration simple has some anomalies and is also confirmed through a low-speed scan in Fig. 4.15. Note that such anomalies are seen as high-frequency signals by the cantilever, and therefore, we expect them to be suitably revealed in the scan obtained using the proposed inner-outer approach. While these anomalies appear sharper in the scans obtained using the proposed approach (Fig. 4.14b), the usual tapping mode image (Fig. 4.14e) contains only faded appearance of them. Moreover, the trace-retrace plot shows that some of the features appear almost *flat* in the usual tapping mode scan. This is also captured by the Bode plot in Fig. 4.10a, where the usual tapping-mode imaging system (with no inner-loop control) has smaller gain at 100Hz, whereas the proposed approach with inner-loop control still has 0dB gain at 100Hz scanning bandwidth.

We now compare the two approaches for the scenario where the two systems have the same 0dB gain at low scanning frequency (60Hz), but exhibit soft engagement between the cantilever tip and the sample (set-point 800mV). As before, the proposed approach highlights features with clearly distinguishable (sharp) boundaries (Fig. 4.14c), while the boundaries are less sharp in the usual tapping-mode scan (Fig. 4.14f). Moreover, some of the features appear *flat* in the trace-retrace plots of the usual tapping-mode scan with large values of trace-retrace mismatch.

4.6 Conclusion

In this chapter, we proposed a control design modification to tapping mode imaging, which resulted in a significant improvement of imaging quality at up to 30% faster speeds. In the next chapter, we address a fundamental limitation of tapping mode imaging by designing a new imaging mode that enables the order of magnitude improvements over tapping mode imaging.

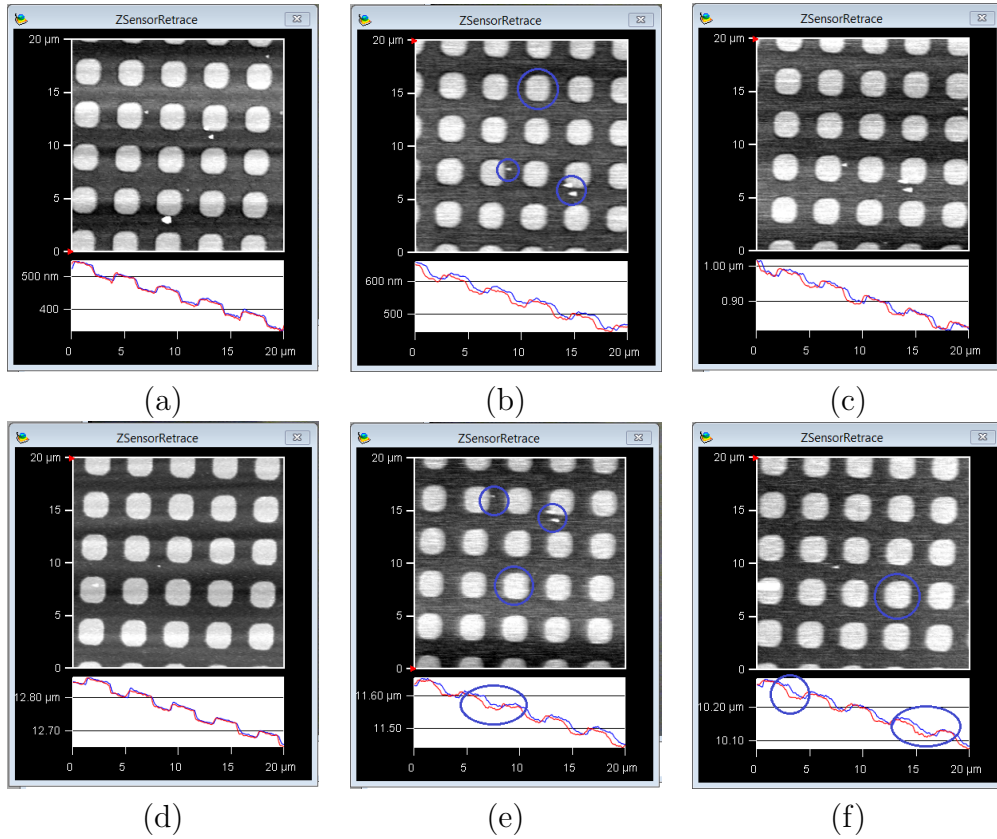


Figure 4.14: Imaging results at different scan-speeds and set-points - with inner-loop control (a) set-point = 600mV, scan-speed = 20 Hz, (b) set-point = 600mV, scan-speed = 100 Hz, (c) set-point = 800mV, scan-speed = 60 Hz; without inner-loop control (d) set-point = 600mV, scan-speed = 20 Hz, (e) set-point = 600mV, scan-speed = 100 Hz, (f) set-point = 800mV, scan-speed = 60 Hz. While the feature heights and shapes, and trace-retrace plots are indistinguishable for a low-speed scan, the proposed control design with modified z -piezo actuator results in improved performance for faster scan and variable set-points. This is seen through the *sharper* features and *better* trace-retrace characteristics.

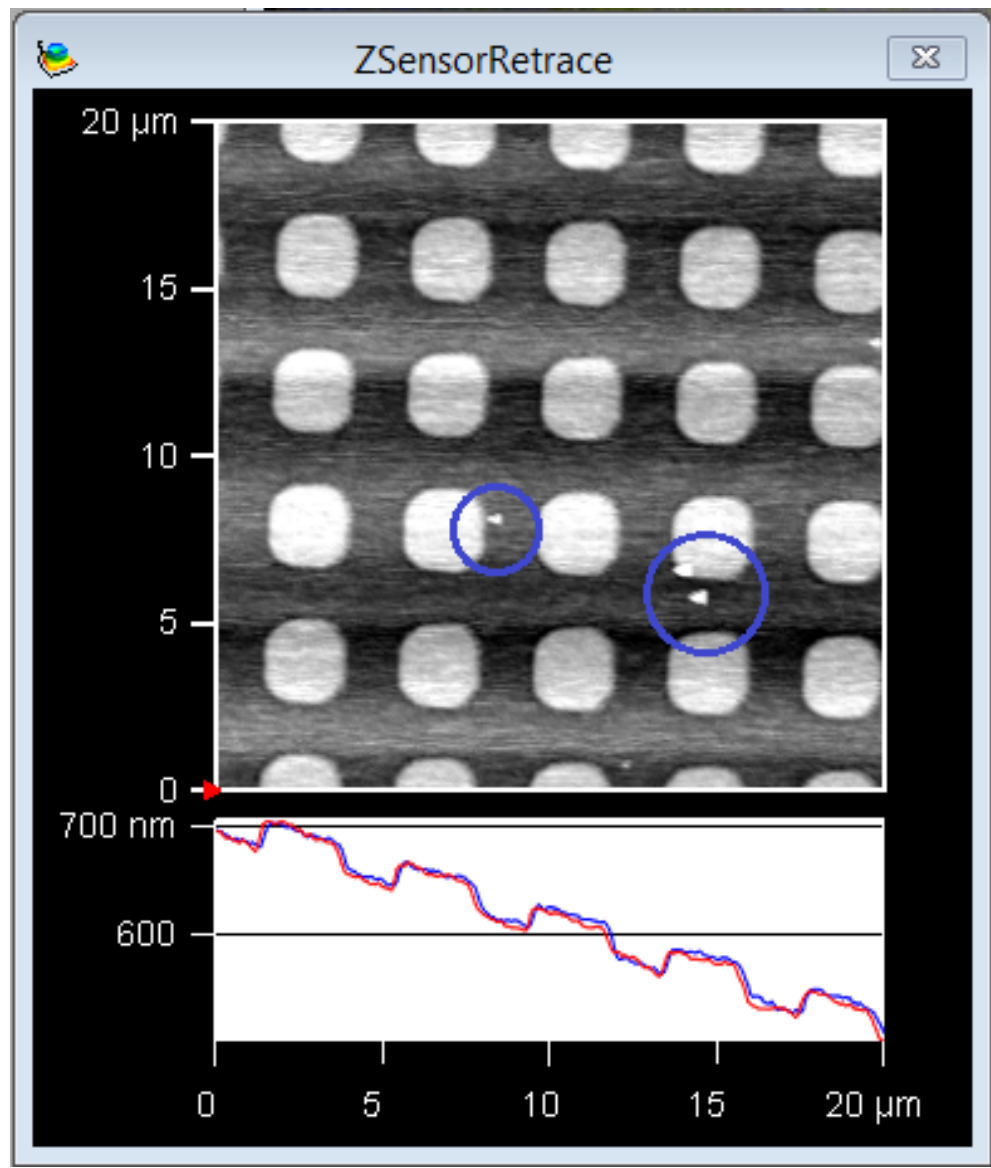


Figure 4.15: Low-speed scan revealing the presence of anomalies in the calibration grating (marked by circles)

CHAPTER 5

A NOVEL TRANSFORM-BASED HIGH-BANDWIDTH AFM IMAGING MODE

While tapping mode imaging is a widely used dynamic imaging mode, it has two characteristics that fundamentally limit the possibility of achieving an order of magnitude improvements in imaging speeds. Firstly, as pointed out in Chapter 4, the sample height to amplitude relationship is uncertain, unknown, and nonlinear. This makes it unsuitable for high bandwidth model-based control designs like \mathcal{H}_∞ control. Thus, tapping mode imaging is performed exclusively using PID controllers. Secondly, tapping mode imaging relies on the amplitude of the deflection signal, which is derived from the deflection signal using an amplitude detection mechanism like peak-detection or lock-in amplifier based detection. Due to the inherent nature of these detection mechanisms, it takes considerable delay, typically around one to two cantilever oscillation cycles, to accurately detect a change in amplitude. This is not a significant concern when the lateral scanning is done at a small percentage of the cantilever resonance frequency. When the lateral scan is done at slow speeds compared to the cantilever resonance frequency, the rate of change of sample features is slow enough to allow for the delay in the detection of amplitude. In other words, the cantilever oscillates over many cycles before sample topography changes considerably. On the other hand, if the lateral positioning speed is high or if the sample surface is extremely rough, the changes in sample topography over a period of cantilever oscillation would be high. This results in a loss of resolution of the image. Due to this issue, the bandwidth of the lateral scan must be very low compared to the cantilever resonance frequency. In practice, for tapping mode imaging, the ratio of lateral scanning bandwidth to the cantilever resonance frequency is about 1% or lower. In this chapter, we use a model-based approach to design a new AFM imaging mode, which can potentially give an order of magnitude improvement in AFM imaging speeds as a ratio of the cantilever resonance frequency.

In order to apply a model-based control design approach, we design a method to mitigate the nonlinear effects in the system model to achieve a high degree of linearity so that tools from robust control theory can be applied to give enhanced performance and robustness. We adopt concepts from an approach that was earlier designed in our lab[15]. The earlier approach developed in our lab seeks to have the cantilever deflection signal track a reference signal. However, upon further analysis, we find that the input-output relationship in the model adopted in that design remains nonlinear to a great extent, making it challenging for effective model-based designs. In this chapter, in addition to seeking to solve an appropriate tracking control problem as in [15], we propose a real-time transform, which, when applied to the output signal, gives a nearly linear input-output relationship. This transform is motivated by the concept of $d - q$ transformation, which is extensively used for the control of power systems. Using the transformed signal as feedback, we design model-based robust controllers, which are shown to achieve significant improvements in system performance in terms of bandwidth of imaging.

5.1 Design Framework

We adopt a model-based design framework for the AFM, where we model the cantilever as a spring-mass-damper system. In our AFM setup, we incorporate a plate piezoelectric element underneath the sample. The plate piezo element has a strain gauge mounted in order to sense its displacement (expansion or contraction) with nanometer resolution. The plate piezo element acts as a very high bandwidth vertical positioning stage that can move the entire sample in the vertical direction. Just as in the case of tapping mode imaging, the cantilever is vibrated close to its natural frequency(ω_n) via an excitation from the dither/shake piezo. It is a well-known fact that the interaction force between the cantilever tip and the sample surface is a highly nonlinear function [18]. The behavior of the AFM cantilever is similar to that of the spring-mass-damper system shown in Fig. 5.1. Let p denote the deflection of the tip of the cantilever, q denote the displacement of the plate piezo, and h denote the sample height.

The dynamics of this cantilever model are described by the following equa-

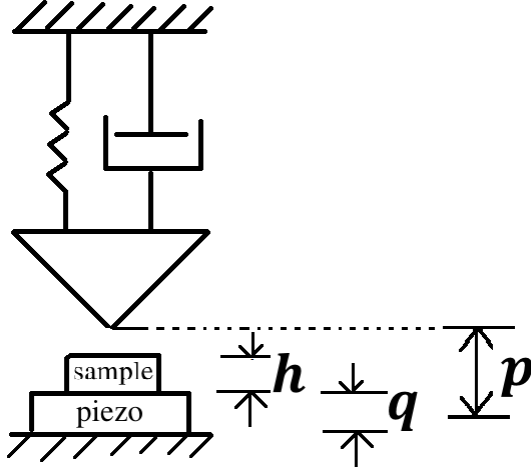


Figure 5.1: Simplified Spring-Mass-Damper model of an AFM cantilever.

tion,

$$\ddot{p} + 2\xi\omega_n\dot{p} + \omega_n^2 p = F_{dither} + F_{ts}(p - q - h), \quad (5.1)$$

where ω_n is the natural frequency of the cantilever, ξ is the damping factor, F_{dither} and F_{ts} are the forces on the cantilever arising due to the dither input and the tip-sample interaction, respectively. As described in chapter 2, the interaction force F_{ts} is a nonlinear function of the tip-sample separation, $p - q - h$. Here, since the dither input is a sinusoidal signal with frequency close to ω_n , due to the linearity of the dither piezo, F_{dither} is also a sinusoidal signal of the same frequency. Now, in the case of regular tapping mode imaging, the amplitude of the dither input is tuned such that the cantilever tip vibrates at a desired amplitude in air. Subsequently, the cantilever position is lowered and regulated close to the sample at a desirable set-point amplitude that is reasonably lower than the free air amplitude chosen above. This regulation is done by regulating the z-stage piezoelectric actuator via a suitable controller that uses the error between the actual amplitude of the tip and the desired amplitude of the tip as a feedback signal. The sample topography is reconstructed from the z-stage displacement and cantilever amplitude signals obtained during a suitable x-y scan of an area of interest on the sample.

For the purpose of imaging faster, instead of using the amplitude signal which has the disadvantage of having to maintain lateral scan speed at less than 1% of the cantilever resonance frequency, we seek to achieve trajectory

tracking of the deflection signal itself. The trajectory to be tracked is chosen to be the trajectory that the cantilever would follow if the sample were to be atomically flat. From the dynamics of the cantilever in (5.1), such a reference trajectory, \hat{p} is governed by the following equation.

$$\ddot{\hat{p}} + 2\xi\omega_n\dot{\hat{p}} + \omega_n^2\hat{p} = F_{dither} + F_{ts}(\hat{p} - h_0), \quad (5.2)$$

where, h_0 is the constant height of the atomically flat sample. We define the tracking error \tilde{p} as

$$\tilde{p} = p - \hat{p} \quad (5.3)$$

From (5.1) and (5.2), the error signal \tilde{p} is governed by the following equation.

$$\ddot{\tilde{p}} + 2\xi\omega_n\dot{\tilde{p}} + \omega_n^2\tilde{p} = F_{ts}(p - q - h) - F_{ts}(\hat{p} - h_0), \quad (5.4)$$

By appropriately choosing the operating point h_0 , for $q = 0$ and when $h = h_0$, the forcing term on the error dynamics is identically zero. Now, for the sake of analysis, let us consider a sample feature with a constant height \tilde{h} about the operating point h_0 , with no actuation, i.e. $q = 0$, the forcing term on the right hand side becomes $F_{ts}(p - (h_0 + \tilde{h})) - F_{ts}(\hat{p} - h_0)$. Since the dynamics of p has the forcing term from the dither signal, with a slight deviation in the sample height, the oscillation of the cantilever will have an amplitude different from that of the reference signal \hat{p} . As a result the forcing term of the error dynamics has dominant frequency components around the resonance frequency of the cantilever. This results in a highly nonlinear relationship between the sample height h and the error signal \tilde{p} . By the same reasoning, the relationship between the actuator displacement q and the error signal \tilde{p} is also highly nonlinear. This makes the system unsuitable for model-based controller design. To overcome this limitation, in the next section, we introduce a transform on the error signal \tilde{p} , which gives a linear relationship from input to the transformed output.

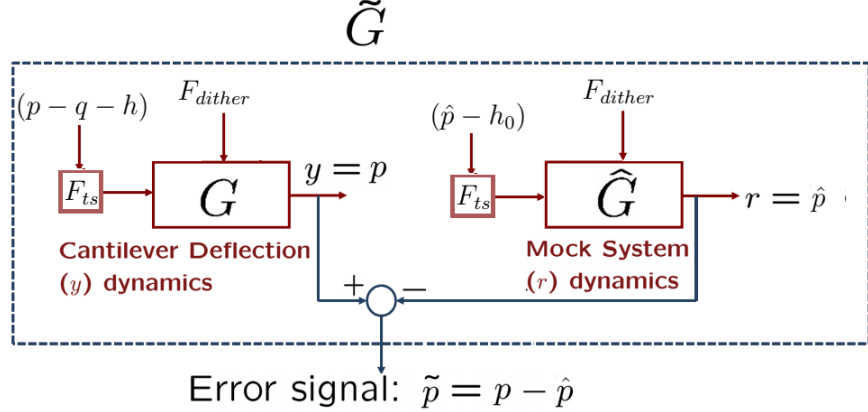


Figure 5.2: Schematic of the error system with \tilde{p} as output

5.2 Real-time frequency shifting transform

In this section, we introduce a real-time frequency shifting transform that has the effect of shifting the frequency of a given signal. Let us consider the signal $\tilde{p}(t)$. Since \tilde{p} is dominated by frequencies around cantilever resonance frequency, ω_n radians per second, we define the corresponding time period T as,

$$T = \frac{2\pi}{\omega_n}.$$

We define the signal $\tilde{p}_\gamma(t)$ as

$$\tilde{p}_\gamma(t) = \tilde{p}(t - T/4).$$

Let,

$$\tilde{P} = \begin{bmatrix} \tilde{p}(t) \\ \tilde{p}_\gamma(t) \end{bmatrix}.$$

Now, we define the transformed signal $\tilde{P}_{\alpha\beta}$ as

$$\tilde{P}_{\alpha\beta} = \begin{bmatrix} \tilde{p}_\alpha(t) \\ \tilde{p}_\beta(t) \end{bmatrix} = \begin{bmatrix} \cos(\omega_n t) & \sin(\omega_n t) \\ -\sin(\omega_n t) & \cos(\omega_n t) \end{bmatrix} \tilde{P}.$$

5.2.1 Analysis of the transformed signal

Suppose, the signal p is a purely sinusoidal signal given by $p(t) = A \cos(\omega_n t + \phi)$. Then, $p_\gamma(t) = p \sin(\omega_n t + \phi)$. And, we have,

$$\begin{aligned} P_{\alpha\beta} &= \begin{bmatrix} A \cos(\omega_n t + \phi) \cos(\omega_n t) - A \sin(\omega_n t + \phi) \sin(\omega_n t) \\ -A \cos(\omega_n t + \phi) \sin(\omega_n t) + A \sin(\omega_n t + \phi) \cos(\omega_n t) \end{bmatrix} \\ &= \begin{bmatrix} A \cos(\phi) \\ A \sin(\phi) \end{bmatrix}. \end{aligned} \quad (5.5)$$

This shows that for a purely sinusoidal signal with frequency ω_n , the transform outputs a constant. In effect, the transform performs the operation of frequency shifting by shifting frequencies at ω_n to zero frequency. Performing this transform in real-time on the error signal \tilde{p} will yield the effect of frequency shifting such that the relationship between the actuator displacement q and the transformed components of the signal \tilde{p} is approximately linear.

Linearity in real-time

To verify the linearity of the relationship between the actuator displacement q and the transformed components of \tilde{p} , we performed simulations with the tip-sample interaction force modeled using the DMT model [18]. Fig.5.3 shows the input signal and the corresponding α -component of the output signal when an input of 20Hz is given to the system shown in Fig.5.2. It can be seen that the α -component of \tilde{p} is periodic, approximately sinusoidal and has the same period as the input signal q . Thus, for a given sinusoidal input, the transform of \tilde{p} is also approximately sinusoidal with the same period. Such kind of behavior can be approximated well by linear transfer function models. Fig. 5.4 shows the frequency responses from q to the β component of the transformed signal for varying amplitudes of white-noise input. It can be seen that the responses of the different cases match closely, indicating a high degree of linearity. Similar behavior was observed for the frequency response from q to the α -component of \tilde{p} as well. Thus, in effect, by making use of this transform along with a carefully chosen reference signal, we are able to mitigate nonlinear effects of the system that are unfavorable for model-based control design. This gives us the platform to exploit the power of robust control theory, which allows us to design controllers that yield a high degree

of robustness and performance. In the next section, we present details of the control design approach we follow.

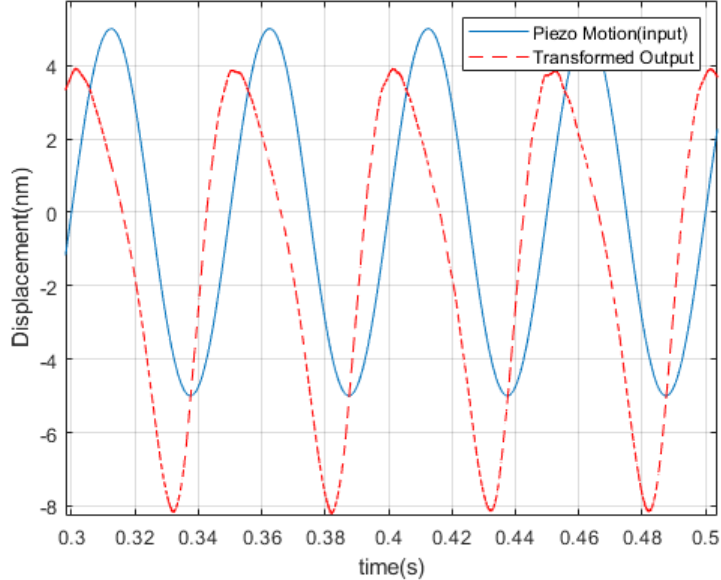


Figure 5.3: Vertical piezo displacement q and the corresponding α -component of \tilde{p} . It can be seen that the α -component of \tilde{p} is periodic, approximately sinusoidal and has the same period as the input signal q

5.3 Control Design

Fig. 5.5 shows the block diagram for the purpose of the control design. G_q represents the transfer function of the plate piezo positioning system on which the sample is mounted from input u_q to output q . \tilde{G} represents the transfer function from the plate piezo displacement q to output \tilde{y} , which is either the α component or the β component of the error signal \tilde{p} , which is obtained by applying the real-time transform discussed in the previous section. The choice of α -component or β -component depends on practical considerations. n represents the measurement noise. The reference signal \tilde{r} is chosen to be zero as the transform of the error tracking zero automatically leads to the error signal \tilde{p} tracking zero. The sample height about the operating point height h_0 , given by \tilde{h} is treated as an input disturbance to be rejected by the controller.

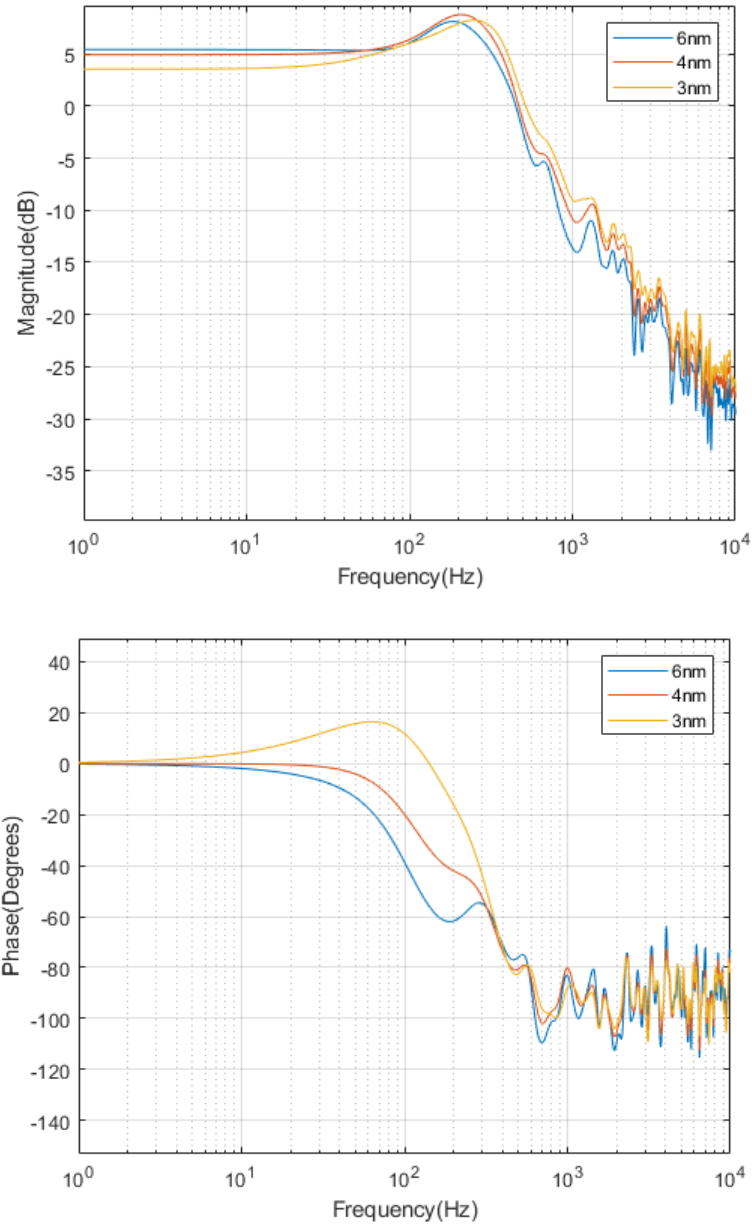


Figure 5.4: Frequency Responses from q to \tilde{p}_β obtained by white-noise identification with three different input amplitudes of 3 nm, 4 nm, and 6 nm. It can be seen that there is a good match between the curves, indicating a high degree of linearity.

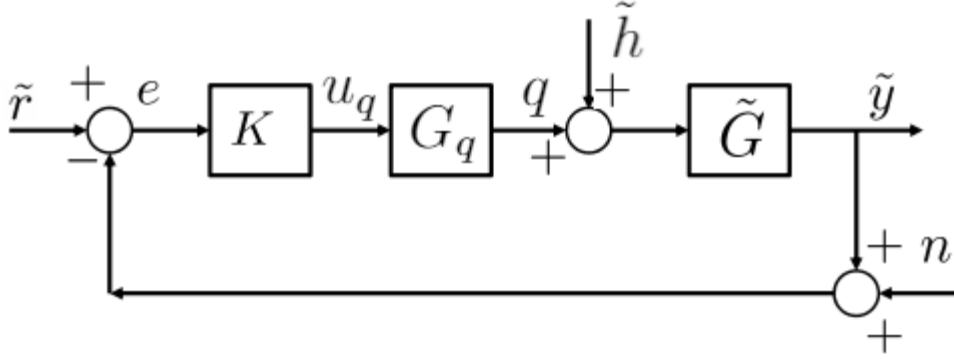


Figure 5.5: Closed-loop feedback diagram: G_q is the transfer function of the plate piezo positioning system with input u_q and output q . \tilde{G} is the transfer function from input q to either one of the α or β components of the transform of \tilde{p} . n represents the measurement noise. \tilde{r} is the reference signal and is chosen to be identically zero, commanding the transform of the error to track zero, which results in error \tilde{p} tracking zero.

We employ the stacked \mathcal{H}_∞ framework to formulate our control objectives. Fig. 5.6(a) shows the closed loop block diagram augmented with the weighting transfer functions w_S , w_T and w_u on the error (e), output(\tilde{y}) and control signal u_q , respectively. The outputs of these transfer function blocks are the exogenous outputs z_1 , z_2 and z_3 . We rewrite all the blocks of this block diagram into the generalized open loop plant P as shown in Fig. 5.6(b). We pose an optimal control problem in order to minimize the \mathcal{H}_∞ norm of the transfer functions from the exogenous inputs \tilde{r} , n and $d = \tilde{h}$ to the exogenous outputs z_1 , z_2 and z_3 .

The required open-loop signals of the generalized plant P are written down from the block diagram Fig. 5.6 as follows.

$$e = -n - \tilde{G}d - \tilde{G}G_q u_q \quad (5.6)$$

$$z_1 = w_S(-n - \tilde{G}d - \tilde{G}G_q u_q) \quad (5.7)$$

$$z_2 = w_u u_q \quad (5.8)$$

$$z_3 = w_T(\tilde{G}d + \tilde{G}G_q u_q) \quad (5.9)$$

Thus, the open-loop generalized plant transfer function for P is given as

follows.

$$\begin{bmatrix} z_1 \\ z_2 \\ z_3 \\ e \end{bmatrix} = \begin{bmatrix} -w_S & -w_S\tilde{G} & -w_S\tilde{G}G_q \\ 0 & 0 & w_u \\ 0 & w_T\tilde{G} & w_T\tilde{G}G_q \\ -1 & -\tilde{G} & -\tilde{G}G_q \end{bmatrix} \begin{bmatrix} n \\ d \\ u_q \end{bmatrix}. \quad (5.10)$$

The closed-loop sensitivity transfer function, S , and complementary sensitivity transfer function, T for the system are as follows.

$$\begin{aligned} S &= \frac{1}{1 + K\tilde{G}G_q}, \\ T &= \frac{K\tilde{G}G_q}{1 + K\tilde{G}G_q} \end{aligned} \quad (5.11)$$

The closed-loop signals relevant for control design are as follows.

$$\begin{aligned} \tilde{y} &= -n + \tilde{G}Sd \\ e &= -Sn - \tilde{G}Sd \\ u_q &= -KSn - K\tilde{G}Sd \end{aligned}$$

The weighting transfer functions w_S and w_T are designed to shape the closed-loop transfer functions S and T such that the solution to the \mathcal{H}_∞ synthesis problem ensures robust stability, disturbance rejection, and noise attenuation. Since $\tilde{G}S$ represents the transfer function from the disturbance signal d to the tracking error e , maximizing the bandwidth of S ensures that the bandwidth of disturbance rejection is maximized. In this case, the bandwidth of S refers to the frequency where Bode plot of the S crosses the -3dB line. In addition, the peak magnitude of S ($\|S\|_\infty$) needs to be minimized in order to keep the tracking error low and ensure robustness to modeling uncertainties and disturbances. Similarly, T represents the transfer function from the noise, n , to the output, y . Hence T must be kept low to ensure good noise attenuation and thus good resolution. Due to the fact that the sum of transfer functions S and T equals unity, both S and T cannot be kept low at the same time. Hence, high resolution is achieved by designing T to have low roll-off frequency and high roll-off rates. This will ensure effective noise attenuation at high frequencies.

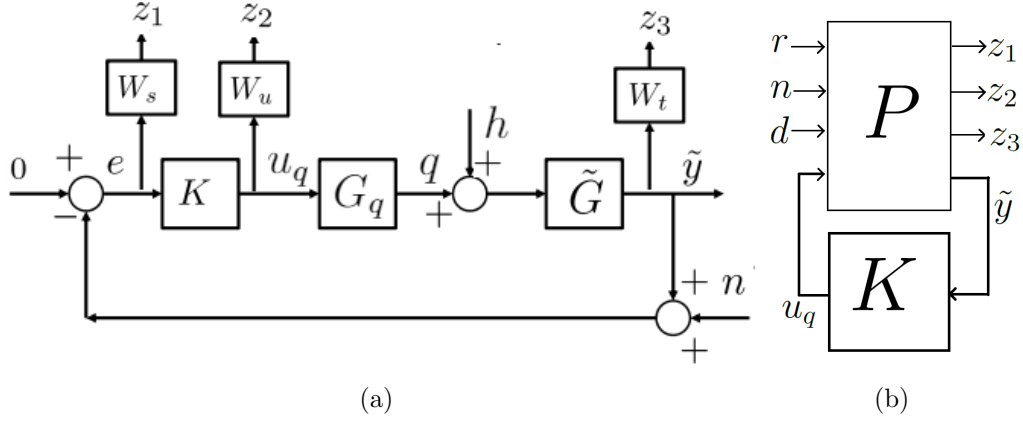


Figure 5.6: (a)Closed-loop system with weighting functions for the stacked \mathcal{H}_∞ control design (b) Open loop generalized plant P with designed controller K . r, n and d are the exogenous inputs. z_1, z_2 and z_3 are the exogenous outputs. K is designed to minimize the \mathcal{H}_∞ norm of the transfer functions from the exogenous inputs to the exogenous outputs

5.4 Simulations

To verify the efficacy of the control design, simulations were performed on a complete model of our AFM system. We used the DMT model to model the tip-sample interactions. However, in experimental implementation, a model will not be needed as experiments based modeling can be used to generate the reference signal \hat{p} . We used the α -component of the transformed error signal as the feedback. Fig. 5.7 shows the closed-loop transfer functions S and T obtained by \mathcal{H}_∞ -optimal control design described in the previous section for a choice of weighting functions. For this design, the Sensitivity transfer function S has a -3 dB bandwidth of 2.69 kHz, with a peak value of 4.22 dB. To illustrate tracking performance for random sample topography, we use filtered white-noise to simulate random sample features. Fig. 5.9(a) shows the tracking performance for a filtered white noise sample topography. It can be seen that the closed-loop system tracks the features almost exactly. Fig. 5.9(b) shows the tracking performance for step input. It can be seen that the closed-loop system tracks the step features almost exactly.

To compare the tracking performance of this controller, we tuned a PID controller to the best possible extent based on the identified linear model. Fig. 5.8 shows the tracking performance of a PID controller, which was tuned to the best possible extent using the linear model of the plant for

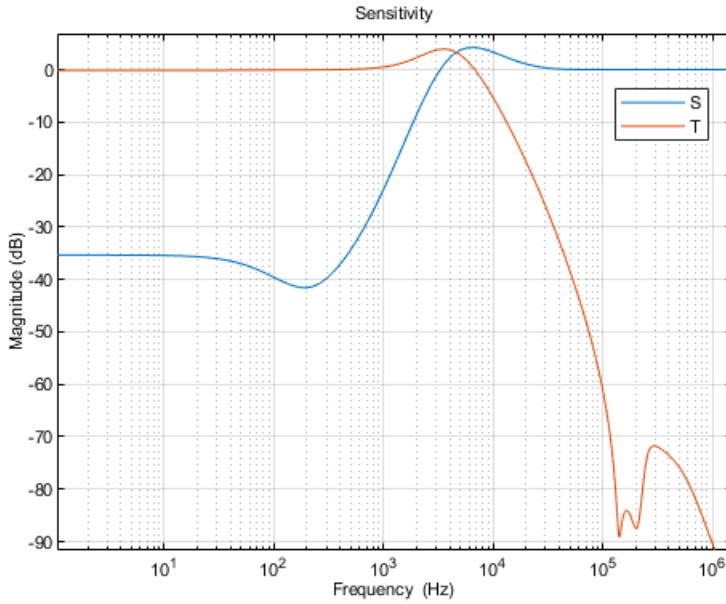


Figure 5.7: Closed-loop transfer functions S and T . The Sensitivity transfer function S has a -3dB bandwidth of 2.69 kHz, with a peak value of 4.22 dB

a 100Hz sine wave. For a 40nm peak-peak amplitude sample feature, We can see that the plate piezo displacement tracks the additive inverse of the sample profile to a great extent with some error at the troughs. However, as we increase the input sine wave frequency, the performance of the PID controller deteriorates, even for smaller feature amplitudes. Fig. 5.10 shows the tracking performance the \mathcal{H}_∞ -optimal controller. For the same 40nm peak-peak amplitude of the sample features, the \mathcal{H}_∞ -optimal controller give near exact tracking at 500 Hz. At 600 Hz, the tracking performance starts to deteriorate but the controller still tracks the features to a great extent. In fact, for smaller feature amplitudes, the tracking performance is even better. 5.11 shows tracking performance of the \mathcal{H}_∞ -optimal controller for 1kHz and 1.2kHz sample profiles with 10nm peak-peak amplitude. Near exact tracking can be seen for features of 1kHz. For features of 1.2 kHz, the tracking performance deteriorates but remains intact to a great extent.

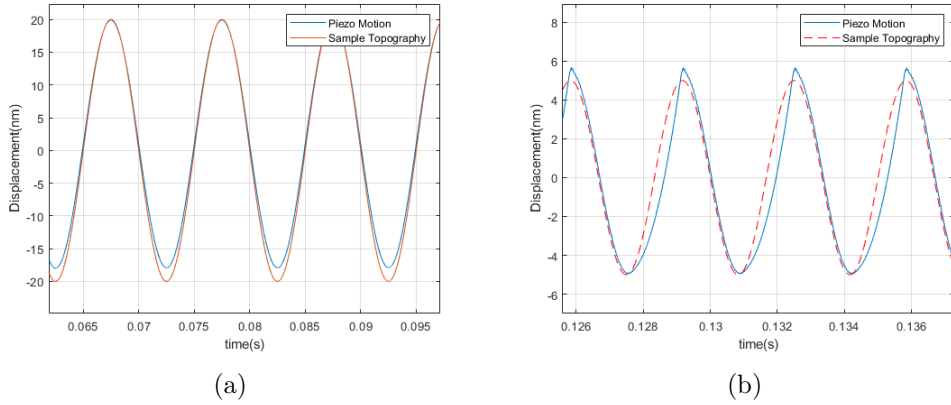


Figure 5.8: Tracking performance of a PID controller with linear model-based tuning (a) for a 100Hz sine wave sample profile with 40nm peak-peak amplitude. The plate piezo displacement (blue) tracks the additive inverse of the sample profile (b) for a 300Hz sine wave sample profile with 10nm peak to peak amplitude. It can be seen that the tracking performance is deteriorated

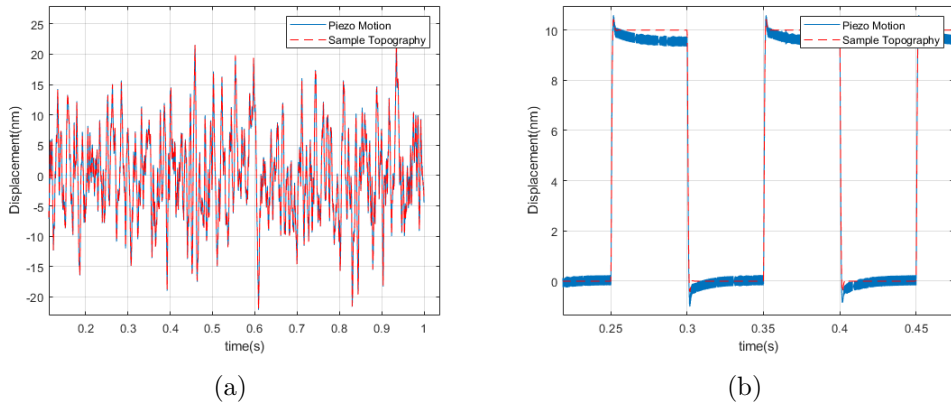


Figure 5.9: Tracking performance of the \mathcal{H}_∞ -optimal controller (a) for filtered white noise sample features. The plate piezo displacement (blue) almost exactly tracks the additive inverse of the sample profile (b) for step features

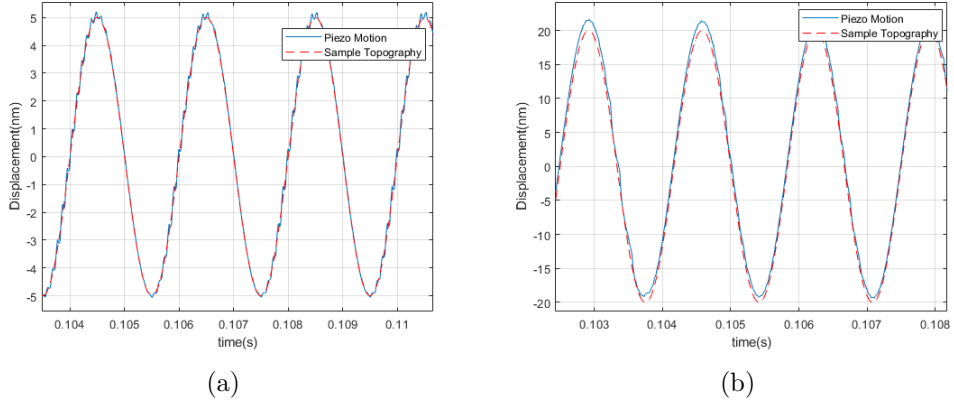


Figure 5.10: Tracking performance of the \mathcal{H}_∞ -optimal controller for 40nm peak-peak amplitude feature (a) for a 500Hz sine wave frequency of sample profile. The plate piezo displacement (blue) almost exactly tracks the additive inverse of the sample profile (b) for a 600Hz sine wave frequency of sample profile. The tracking performance starts deteriorating but still remains intact to a good extent

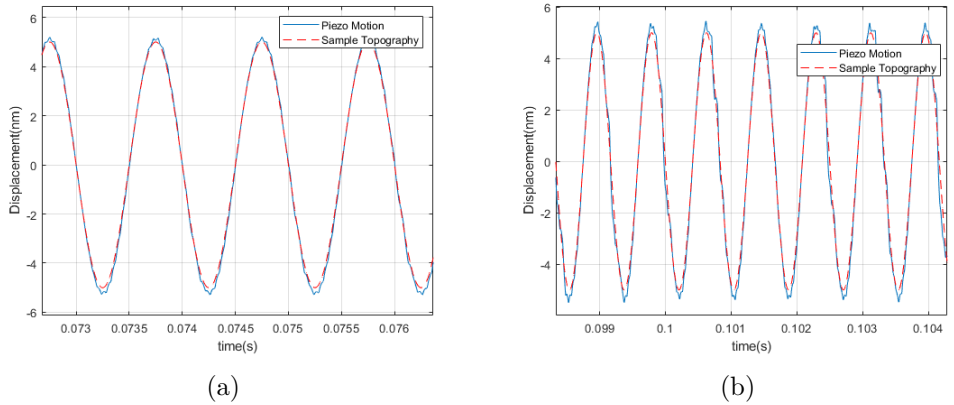


Figure 5.11: Tracking performance of the \mathcal{H}_∞ -optimal controller for 10nm peak-peak amplitude feature (a) for a 1kHz sine wave frequency of sample profile. The plate piezo displacement (blue) almost exactly tracks the additive inverse of the sample profile (b) for a 1.2kHz sine wave frequency of sample profile. The tracking performance starts deteriorating but still remains intact to a good extent

5.5 Conclusion

In this chapter, we described a transform-based method that gives a nearly linear relationship between the sample topography signal and the output signal. This method was used to design a new AFM imaging mode that relies directly on the deflection signal rather than a slower derivative such as amplitude or phase. The initial results obtained by this method show the efficacy of Robust \mathcal{H}_∞ optimal control designs for High-Bandwidth imaging. \mathcal{H}_∞ optimal controllers are shown to give at least a six times improvement over PID controller tuned to the best possible extent. This indicates that higher performance can be achieved by careful use of robust control designs.

CHAPTER 6

CONCLUSIONS AND FUTURE DIRECTIONS

This dissertation has developed methods for enabling fast imaging in AFMs. We have successfully integrated hardware capabilities for proof of concept studies on systems-based approaches in AFMs. In tapping mode imaging, we have incorporated the sensor of the vertical nanopositioning system, which has a lower resolution than the deflection sensor. By employing appropriately designed model-based control strategies, we could experimentally realize up to 30% improvements in tapping mode imaging speeds.

Tapping mode imaging is fundamentally limited by the requirement that lateral positioning needs to be a small percentage, in the order of 1% of the cantilever resonance frequency. We proposed a transform-based high-bandwidth imaging mode that shows a linear input-output relationship. The proposed mode has been shown to be effective by showing that the vertical nanopositioner motion effectively tracks the additive inverse of the sample topography profile. Careful design of robust \mathcal{H}_∞ -optimal controller would yield further improvements in imaging bandwidth. The high-bandwidth imaging mode proposed in this thesis shows promise in achieving improvements of an order of magnitude over tapping mode imaging. Further research efforts are needed to analyze further and improve the proposed imaging mode, including studying the effect of the choice of α -component or β -component for feedback. Cascaded control design ideas on the vertical nanopositioning stage G_q might further enhance the performance of the proposed imaging mode and is a candidate for further study. Experimental implementation of the proposed imaging mode will be an immediate near term goal. An extensive comparison with tapping mode imaging is needed to quantify the improvements in imaging bandwidth. The methods outlined in [15] can be used to estimate the material properties of the sample surface in conjunction with the proposed imaging mode for topography imaging. In current tapping mode imaging, the cantilever tip spends a good fraction of oscillation time outside the re-

gion of influence of tip-sample interaction forces. Low-amplitude imaging will provide enhanced sensitivity and hence better resolutions at high-speeds of imaging.

Research in this thesis has shown that systems-based control design approaches hold great promise in delivering high performance and robustness in AFM imaging. We have shown that considerable improvements as large as 30% in performance can be achieved by analyzing and designing controllers for AFMs from a systems viewpoint. Advances in nanopositioning device bandwidths have opened up the possibility of fast lateral and vertical scanning in AFM nanopositioners. Tools from advanced control theory can aid in fully harnessing the capabilities of these devices and also pushing the limits on AFM imaging bandwidths. Advances in reconfigurable computing continue to enable the feasibility of implementing advanced control designs in real-time.

REFERENCES

- [1] G. Binnig, C. F. Quate, and C. Gerber, “Atomic force microscope,” *Phys. Rev. Lett.*, vol. 56, pp. 930–933, Mar 1986.
- [2] F. J. Giessibl, “Atomic resolution of the silicon (111)-(7x7) surface by atomic force microscopy,” *Science*, vol. 267, no. 5194, pp. 68–71, 1995.
- [3] A. Extance, “How atomic imaging is being pushed to its limit,” *Nature*, vol. 555, pp. 545–547, 03 2018.
- [4] T. Ando, “Molecular machines directly observed by high-speed atomic force microscopy,” *FEBS Letters*, vol. 587, no. 8, pp. 997 – 1007, 2013. The many faces of proteins.
- [5] O. D. Payton, L. Picco, and T. B. Scott, “High-speed atomic force microscopy for materials science,” *International Materials Reviews*, vol. 61, no. 8, pp. 473–494, 2016.
- [6] T. Ashley, T. Huang, W. Nagel, S. Andersson, and K. Leang, “High speed afm through non-raster scanning and high speed actuation,” *Bioophysical Journal*, vol. 110, pp. 500a–501a, 02 2016.
- [7] N. Nikooienejad, A. Alipour, M. Maroufi, and S. R. Moheimani, “Video-rate non-raster afm imaging with cycloid trajectory,” *IEEE Transactions on Control Systems Technology*, 2018.
- [8] A. Bazaei, M. Maroufi, A. G. Fowler, and S. O. R. Moheimani, “Internal model control for spiral trajectory tracking with mems afm scanners,” *IEEE Transactions on Control Systems Technology*, vol. 24, no. 5, pp. 1717–1728, 2016.
- [9] T. Tuma, J. Lygeros, V. Kartik, A. Sebastian, and A. Pantazi, “High-speed multiresolution scanning probe microscopy based on lissajous scan trajectories,” *Nanotechnology*, vol. 23, p. 185501, 05 2012.
- [10] M. Lutwyche, C. Andreoli, G. Binnig, J. Brugger, U. Drechsler, W. Häberle, H. Rohrer, H. Rothuizen, P. Vettiger, G. Yaralioglu, *et al.*, “5× 5 2d afm cantilever arrays a first step towards a terabit storage

- device,” *Sensors and Actuators A: Physical*, vol. 73, no. 1-2, pp. 89–94, 1999.
- [11] P. Vettiger, J. Brugger, M. Despont, U. Drechsler, U. Dürig, W. Häberle, M. Lutwyche, H. Rothuizen, R. Stutz, R. Widmer, *et al.*, “Ultrahigh density, high-data-rate nems-based afm data storage system,” *Micro-electronic Engineering*, vol. 46, no. 1-4, pp. 11–17, 1999.
 - [12] A. Ahmad, N. Nikolov, T. Angelov, T. Ivanov, A. Reum, I. Atanasov, E. Guliyev, V. Ishchuk, M. Kaestner, Y. Krivoshapkina, *et al.*, “Large area fast-afm scanning with active “quattro” cantilever arrays,” *Journal of Vacuum Science & Technology B, Nanotechnology and Microelectronics: Materials, Processing, Measurement, and Phenomena*, vol. 34, no. 6, p. 06KM03, 2016.
 - [13] S. Skogestad and I. Postlethwaite, *Multivariable feedback control: analysis and design*, vol. 2. Wiley, 2010.
 - [14] D. McFarlane and K. Glover, “A loop-shaping design procedure using \mathcal{H}_∞ synthesis,” *Automatic Control, IEEE Transactions on*, vol. 37, no. 6, pp. 759–769, 1992.
 - [15] G. Mohan, *A new dynamic mode for fast imaging in atomic force microscopes*. PhD thesis, University of Illinois, Urbana-Champaign, 2013.
 - [16] G. Binnig, H. Rohrer, C. Gerber, and E. Weibel, “Tunneling through a controllable vacuum gap,” *Applied Physics Letters*, vol. 40, no. 2, pp. 178–180, 1982.
 - [17] S. M. SALAPAKA and M. V. SALAPAKA, “Scanning probe microscopy,” *IEEE Control Systems Magazine*, vol. 28, pp. 65–83, April 2008.
 - [18] B. Derjaguin, V. Muller, and Y. Toporov, “Effect of contact deformations on the adhesion of particles,” *Journal of Colloid and Interface Science*, vol. 53, no. 2, pp. 314 – 326, 1975.
 - [19] K. L. Johnson, K. Kendall, and a. Roberts, “Surface energy and the contact of elastic solids,” *Proceedings of the royal society of London. A. mathematical and physical sciences*, vol. 324, no. 1558, pp. 301–313, 1971.
 - [20] C. Lee and S. M. Salapaka, “Robust broadband nanopositioning: fundamental trade-offs, analysis, and design in a two-degree-of-freedom control framework,” *Nanotechnology*, vol. 20, p. 035501, dec 2008.
 - [21] S. Salapaka, A. Sebastian, J. Cleveland, and M. Salapaka, “Design, identification and control of a fast nanopositioning device,” vol. 3, pp. 1966 – 1971 vol.3, 02 2002.

- [22] S. Polit and J. Dong, “Development of a high-bandwidth xy nanopositioning stage for high-rate micro-/nanomanufacturing,” *IEEE/ASME Transactions on Mechatronics*, vol. 16, pp. 724–733, Aug 2011.
- [23] C. Preissner, J. Deng, C. Jacobsen, B. Lai, F. Marin, J. Maser, S. Mashrafi, C. Roehrig, S. Sullivan, and S. Vogt, “Earth, Wind, and Fire: The New Fast Scanning Velociprobe,” in *Proceedings, 9th Mechanical Engineering Design of Synchrotron Radiation Equipment and Instrumentation (MEDSI 2016): Barcelona, Spain, September 11-16, 2016*, p. TUAA02, 2017.
- [24] G. Schitter, K. J. Astrom, B. E. DeMartini, P. J. Thurner, K. L. Turner, and P. K. Hansma, “Design and modeling of a high-speed afm-scanner,” *IEEE Transactions on Control Systems Technology*, vol. 15, pp. 906–915, Sep. 2007.
- [25] J. Dong, S. M. Salapaka, and P. M. Ferreira, “Robust mimo control of a parallel kinematics nano-positioner for high resolution high bandwidth tracking and repetitive tasks,” in *2007 46th IEEE Conference on Decision and Control*, pp. 4495–4500, Dec 2007.
- [26] B. J. Kenton and K. K. Leang, “Design and control of a three-axis serial-kinematic high-bandwidth nanopositioner,” *IEEE/ASME Transactions on Mechatronics*, vol. 17, pp. 356–369, April 2012.
- [27] C. Lee and S. M. Salapaka, “Robust broadband nanopositioning: fundamental trade-offs, analysis, and design in a two-degree-of-freedom control framework,” *Nanotechnology*, vol. 20, no. 3, p. 035501, 2009.
- [28] S. Skogestad and I. Postlethwaite, *Multivariable feedback control: analysis and design - Chapters 2, 5, 8 and 9*, vol. 2. Wiley New York, 2007.
- [29] S. R. Moheimani, “Invited review article: Accurate and fast nanopositioning with piezoelectric tube scanners: Emerging trends and future challenges,” *Review of Scientific Instruments*, vol. 79, no. 7, p. 071101, 2008.
- [30] G. W. Johnson, *LabVIEW Graphical Programming: Practical Applications in Instrumentation and Control*. Hauptbd. McGraw-Hill, 1994.
- [31] “Ni x series multifunction data acquisition.” <http://www.ni.com/datasheet/pdf/en/ds-151>.
- [32] J. C. Doyle, B. A. Francis, and A. Tannenbaum, *Feedback control theory - Chapters 11, 12*, vol. 1. Macmillan Publishing Company New York, 1992.

- [33] K. Glover and D. McFarlane, “Robust stabilization of normalized coprime factor plant descriptions with H_∞ -bounded uncertainty,” *Automatic Control, IEEE Transactions on*, vol. 34, no. 8, pp. 821–830, 1989.
- [34] A. Sebastian and S. M. Salapaka, “Design methodologies for robust nano-positioning,” *Control Systems Technology, IEEE Transactions on*, vol. 13, no. 6, pp. 868–876, 2005.
- [35] M. Vidyasagar, *Control system synthesis: a factorization approach - Chapter 4*. Morgan & Claypool Publishers, 2011.
- [36] L. Ljung, “System identification: Theory for the user,” *PTR Prentice Hall Information and System Sciences Series*, vol. 198, 1987.
- [37] G. E. Dullerud and F. Paganini, *A course in robust control theory: a convex approach*, vol. 36. Springer Science & Business Media, 2013.
- [38] *Field Programmable Analog Array: AN231K04-DVLP3 - AnadigmApex Development Board*. Anadigm Inc., Campbell, CA, USA, 2006.
- [39] P25M, “<http://www.innovative-dsp.com/products.php?product=p25m>,” *Innovative Integration*.
- [40] AC240TS, “<http://www.asylumresearch.com/probe/ac240ts,olympus>,” *Olympus*.
- [41] *Contact-G*. Budget Sensors.
- [42] S. M. Salapaka, T. De, and A. Sebastian, “New approaches for sample-profile estimation for fast atomic force microscopy,” in *ASME 2005 International Mechanical Engineering Congress and Exposition*, pp. 1317–1326, American Society of Mechanical Engineers, 2005.
- [43] R. S. Gorugantu and S. M. Salapaka, “A new dynamic imaging mode for high-resolution and high-bandwidth atomic force microscopy,” in *2018 Annual American Control Conference (ACC)*, pp. 6018–6023, June 2018.
- [44] M. Baranwal, R. S. Gorugantu, and S. M. Salapaka, “Robust atomic force microscopy using multiple sensors,” *Review of Scientific Instruments*, vol. 87, no. 8, p. 083704, 2016.
- [45] M. Baranwal, R. S. Gorugantu, and S. M. Salapaka, “Fast and robust control of nanopositioning systems: Performance limits enabled by field programmable analog arrays,” *Review of Scientific Instruments*, vol. 86, no. 8, p. 085004, 2015.

- [46] G. Mohan, C. Lee, and S. Salapaka, “Control techniques for high-speed dynamic mode imaging in atomic force microscopes,” in *2011 50th IEEE Conference on Decision and Control and European Control Conference*, pp. 651–656, Dec 2011.
- [47] B. Voigtländer, *Scanning Probe Microscopy*. Springer Berlin, 2016.
- [48] S. Salapaka, T. De, and A. Sebastian, “Sample-profile estimate for fast atomic force microscopy,” *Applied Physics Letters*, vol. 87, no. 5, p. 053112, 2005.
- [49] C. Lee and S. M. Salapaka, “Fast imaging with alternative signal for dynamic atomic force microscopy,” *Applied Physics Letters*, vol. 97, no. 13, p. 133101, 2010.
- [50] J. D. Adams, B. W. Erickson, J. Grossenbacher, J. Brugger, A. Nieveldt, and G. E. Fantner, “Harnessing the damping properties of materials for high-speed atomic force microscopy,” *Nature Nanotechnology*, vol. 11, pp. 147 EP –, Nov 2015.
- [51] G. Binnig, C. F. Quate, and C. Gerber, “Atomic force microscope,” *Physical review letters*, vol. 56, no. 9, p. 930, 1986.
- [52] Y. Sugimoto, P. Pou, O. Custance, P. Jelinek, M. Abe, R. Perez, and S. Morita, “Complex patterning by vertical interchange atom manipulation using atomic force microscopy,” *Science*, vol. 322, no. 5900, pp. 413–417, 2008.
- [53] A. Dazzi, C. B. Prater, Q. Hu, D. B. Chase, J. F. Rabolt, and C. Marcott, “Afm-ir: combining atomic force microscopy and infrared spectroscopy for nanoscale chemical characterization,” *Applied spectroscopy*, vol. 66, no. 12, pp. 1365–1384, 2012.
- [54] H. Sugimura and N. Nakagiri, “Afm lithography in constant current mode,” *Nanotechnology*, vol. 8, no. 3A, p. A15, 1997.
- [55] N. Kodera, D. Yamamoto, R. Ishikawa, and T. Ando, “Video imaging of walking myosin v by high-speed atomic force microscopy,” *Nature*, vol. 468, no. 7320, pp. 72–76, 2010.
- [56] M. Kitazawa, K. Shiotani, and A. Toda, “Batch fabrication of sharpened silicon nitride tips,” *Japanese journal of applied physics*, vol. 42, no. 7S, p. 4844, 2003.
- [57] T. Ando, “High-speed atomic force microscopy coming of age,” *Nanotechnology*, vol. 23, no. 6, p. 062001, 2012.
- [58] “Family overview,” *Anadigm*, 2003.

- [59] S. Bains, “Analog’s answer to fpga opens field to masses,” *EE Times*, vol. 1510, p. 1, 2008.
- [60] MATLAB, *version 7.10.0 (R2010a)*. Natick, Massachusetts: The MathWorks Inc., 2010.
- [61] M. Baranwal, “Application of field programmable analog arrays (fpaas) to fast scanning probe microscopy,” 2014.
- [62] S. Salapaka, B. Johnson, B. Lundstrom, S. Kim, S. Collyer, and M. Salapaka, “Viability and analysis of implementing only voltage-power droop for parallel inverter systems,” in *Decision and Control (CDC), 2014 IEEE 53rd Annual Conference on*, pp. 3246–3251, IEEE, 2014.
- [63] C. Lee and S. M. Salapaka, “Fast imaging with alternative signal for dynamic atomic force microscopy,” *Applied Physics Letters*, vol. 97, no. 13, pp. 133101–133101, 2010.
- [64] C. Lee and S. Salapaka, “A new sample-profile estimation signal in dynamic-mode atomic force microscopy,” in *Mechatronic Systems*, pp. 232–239, 2010.
- [65] M. Baranwal, R. S. Gorugant, and S. M. Salapaka, “Fast and robust control of nanopositioning systems: Performance limits enabled by field programmable analog arrays,” *Review of Scientific Instruments*, vol. 86, no. 8, p. 085004, 2015.
- [66] D. Rugar and P. Hansma, “Atomic force microscopy,” *Physics today*, vol. 43, no. 10, pp. 23–30, 1990.
- [67] S. Pennycook and S. Kalinin, “Microscopy: Hasten high resolution,” *Nature*, vol. 515, pp. 487–8, 11 2014.
- [68] F. J. Giessibl, “Advances in atomic force microscopy,” *Reviews of modern physics*, vol. 75, no. 3, p. 949, 2003.
- [69] K. S. Karvinen, M. G. Ruppert, K. Mahata, and S. R. Moheimani, “Direct tip-sample force estimation for high-speed dynamic mode atomic force microscopy,” *Nanotechnology, IEEE Transactions on*, vol. 13, no. 6, pp. 1257–1265, 2014.
- [70] G. Schitter, R. Stark, and A. Stemmer, “Fast contact-mode atomic force microscopy on biological specimen by model-based control,” *Ultramicroscopy*, vol. 100, no. 3, pp. 253–257, 2004.
- [71] C. B. Lee and G. Mohan, “New estimation method of sample properties in dynamic afm,” in *Advanced Materials Research*, vol. 684, pp. 377–380, Trans Tech Publ, 2013.

- [72] S. Devasia, E. Eleftheriou, and S. R. Moheimani, “A survey of control issues in nanopositioning,” *Control Systems Technology, IEEE Transactions on*, vol. 15, no. 5, pp. 802–823, 2007.
- [73] S. Salapaka, A. Sebastian, J. P. Cleveland, and M. V. Salapaka, “High bandwidth nano-positioner: A robust control approach,” *Review of scientific instruments*, vol. 73, no. 9, pp. 3232–3241, 2002.
- [74] A. Sebastian and S. Salapaka, “ \mathcal{H}_∞ loop shaping design for nanopositioning,” in *American Control Conference, 2003. Proceedings of the 2003*, vol. 5, pp. 3708–3713, IEEE, 2003.
- [75] C. Lee and S. M. Salapaka, “Fast robust nanopositioning—a linear-matrix-inequalities-based optimal control approach,” *Mechatronics, IEEE/ASME Transactions on*, vol. 14, no. 4, pp. 414–422, 2009.
- [76] A. J. Fleming, S. S. Aphale, and S. R. Moheimani, “A new method for robust damping and tracking control of scanning probe microscope positioning stages,” *Nanotechnology, IEEE Transactions on*, vol. 9, no. 4, pp. 438–448, 2010.
- [77] A. Gannepalli, A. Sebastian, J. P. Cleveland, and M. V. Salapaka, “Thermal noise response based control of tip-sample separation in afm,” in *American Control Conference, 2004. Proceedings of the 2004*, vol. 4, pp. 3122–3127, IEEE, 2004.
- [78] D. R. Sahoo, T. De Murti, and M. V. Salapaka, “Observer based imaging methods for atomic force microscopy,” in *Decision and Control, 2005 and 2005 European Control Conference. CDC-ECC’05. 44th IEEE Conference on*, pp. 1185–1190, IEEE, 2005.
- [79] A. Sarwar, P. G. Voulgaris, and S. M. Salapaka, “On the control design and robustness analysis for high-density microcantilever arrays,” *Journal of Vibration and Control*, p. 1077546310381038, 2010.
- [80] M. Napoli, B. Bamieh, and M. Dahleh, “Optimal control of arrays of microcantilevers,” *Journal of dynamic systems, measurement, and control*, vol. 121, no. 4, pp. 686–690, 1999.
- [81] P. Vettiger, M. Despont, U. Drechsler, U. Dürig, W. Häberle, M. I. Lutwyche, H. E. Rothuizen, R. Stutz, R. Widmer, and G. K. Binnig, “The “millipede”—more than thousand tips for future afm storage,” *IBM Journal of Research and Development*, vol. 44, no. 3, pp. 323–340, 2000.
- [82] D. Walters, J. Cleveland, N. Thomson, P. Hansma, M. Wendman, G. Gurley, and V. Elings, “Short cantilevers for atomic force microscopy,” *Review of Scientific Instruments*, vol. 67, no. 10, pp. 3583–3590, 1996.

- [83] B. J. Kenton and K. K. Leang, “Design and control of a three-axis serial-kinematic high-bandwidth nanopositioner,” *Mechatronics, IEEE/ASME Transactions on*, vol. 17, no. 2, pp. 356–369, 2012.
- [84] S. P. Wadikhaye, Y. K. Yong, and S. Reza Moheimani, “Design and characterisation of a serial-kinematic nanopositioner for high-speed afm,” in *Advanced Intelligent Mechatronics (AIM), 2014 IEEE/ASME International Conference on*, pp. 210–215, IEEE, 2014.
- [85] B. Rogers, L. Manning, T. Sulchek, and J. Adams, “Improving tapping mode atomic force microscopy with piezoelectric cantilevers,” *Ultramicroscopy*, vol. 100, no. 3, pp. 267–276, 2004.
- [86] P. Huang and S. B. Andersson, “High speed atomic force microscopy enabled by a sample profile estimator,” *Applied physics letters*, vol. 102, no. 21, p. 213118, 2013.
- [87] Y. Luo and S. B. Andersson, “A fast image reconstruction algorithm for compressed sensing-based atomic force microscopy,” in *American Control Conference (ACC), 2015*, pp. 3503–3508, IEEE, 2015.
- [88] T. Tuma, W. Haeberle, H. Rothuizen, J. Lygeros, A. Pantazi, and A. Sebastian, “Dual-stage nanopositioning for high-speed scanning probe microscopy,” *Mechatronics, IEEE/ASME Transactions on*, vol. 19, no. 3, pp. 1035–1045, 2014.
- [89] Y. K. Yong and S. Moheimani, “Collocated z-axis control of a high-speed nanopositioner for video-rate atomic force microscopy,” *Nanotechnology, IEEE Transactions on*, vol. 14, no. 2, pp. 338–345, 2015.
- [90] A. C. Shegaonkar and S. M. Salapaka, “Feedback based simultaneous correction of imaging artifacts due to geometrical and mechanical cross-talk and tip-sample stick in atomic force microscopy,” *Review of Scientific Instruments*, vol. 78, no. 10, p. 103706, 2007.